DEPARTMENT OF ECONOMICS,
MANAGEMENT AND STATISTICS

UNIVERSITY OF MILAN – BICOCCA

DEMS WORKING PAPER SERIES

Temperature anomalies, radiative forcing and ENSO

Claudio Morana and Giacomo Sbrana

No. 361 – February 2017
Revised version: June 2017

Dipartimento di Economia, Metodi Quantitativi e Strategie di Impresa
Università degli Studi di Milano - Bicocca
http://dems.unimib.it/

Temperature anomalies, radiative forcing and ENSO*

Claudio Morana*†, Giacomo Sbrana+

*Università di Milano Bicocca, CeRP-Collegio Carlo Alberto (Moncalieri, Italy)
and Rimini Centre for Economic Analysis (Rimini, Italy).

+NEOMA Business School

June 2017

Abstract

The paper investigates the linkages between temperature anomalies, radiative forcing and ENSO. By means of a new flexible trend modeling approach, we uncover a nonlinear linkage between radiative forcing and global temperature anomalies. The nonlinear trend closely tracks the low frequency evolution in temperature anomalies, also accounting for the mid-end 1990s level switch, the 1998-2013 "warming hiatus" and the current steepening in trend temperatures. Radiative forcing is also found to account for trend dynamics in the Southern Oscillation Index (SOI), therefore providing support for the view that global warming might affect natural variability oscillations such as ENSO, and therefore enhance their disruptive effects. We also document the feature of time-varying volatility of temperature anomalies and SOI, which is well described by an IGARCH process. By means of a new dynamic conditional correlation model (SP-DCC), we finally document the presence of time-varying conditional correlations relating temperature anomalies across various zones and SOI. The correlation pattern is found to be consistent with the effects of ENSO events in the Tropics and their teleconnections.

Keywords: Temperature anomaly, global warming, warming hiatus, radiative forcing, ENSO, El Niño, conditional heteroskedasticity, semiparametric dynamic conditional correlation model.
JEL classification: C32

*The paper was previously circulated with the title "Modeling time varying volatility and correlations in temperature anomalies". The paper was presented at the Conference on Econometric Models of Climate Change (Aarhus University). The authors are grateful to conference participants for constructive comments.

†Address for correspondence: Claudio Morana, Università di Milano-Bicocca, Dipartimento di Economia, Metodi Quantitativi e Strategie di Impresa, Piazza dell'Ateneo Nuovo 1, 20126, Milano, Italy. E-mail: claudio.morana@unimib.it.

1 Introduction

El Niño events refer to the warm and negative phases of the El Niño Southern Oscillation (ENSO) and are the warming of the ocean surface or above-average sea surface temperatures in either the central and eastern tropical Pacific Ocean. This warming causes a shift in the atmospheric circulation with rainfall decreasing over Indonesia and Australia, while rainfall and tropical cyclone formation rises over the tropical Pacific Ocean, i.e. from Mexico to Chile. While El Niño events have been occurring for thousands of years, and at least 30 of them since 1900, the 1982-1983, 1997-1998 and 2014-2016 events are among the strongest recorded so far. The 2014-2016 event heavily influenced tropical cyclone activity around the world, contributing to the most active tropical cyclone season on record for the Central Pacific basin and, also due to the effects of the concurrent positive Indian Ocean Dipole (IOD), to the least active tropical cyclone season in the Australian region. It contributed also to the formation of some systems outside of the season boundaries within the North Atlantic, Eastern and Southern Pacific basins. Various countries around the world, including Africa, Central America, South-East Asia and Pacific Islands, were affected by below or above-average rainfall and flooding; increased food scarcity, malnutrition and devastated livelihoods, increased susceptibility to illnesses, and forced displacement (UNOCHA, 2016).[1]

As El Niño events affect the global climate and disrupts normal weather patterns, they might be a likely candidate to account for changing temperature anomalies in various geographical areas. In this respect, Jones (1989) and Wigley (2000) find that following a typical El Niño event the global surface air temperature increases of up 0.1 C with a lag of 6 months. A larger impact of 0.2 C is documented by Christy and McNider (1994) and Angell (2000) in correspondence of the 1997-1998 very strong El Niño event. ENSO is essentially an asymmetric phenomenon: as pointed out by Cai et al. (2015a,b; 2014) and Kim et al. (2014), extreme ENSO events are different from moderate events and in assessing the impact of global warning the latter events should then be kept separate.

The consensus view on the contribution of ENSO to global warming posits, however, that ENSO might account for between 10% and 30% of the interseasonal and longer-term change in surface and/or lower tropospheric temperature, but little of the global mean warming trend since the 1950s (Foster et al., 2009).[2] The latter warming trend is generally related to radiative forcing, both of natural and anthropogenic origin, whose stochastic or deterministic nature has been contended in the literature since the early 1990s. On the one hand, recent contributions such as Kaufmann et al. (2013) and Schmith et al. (2012) point to a stochastic trend in global and Northern (NH) and Southern (SH) hemisphere temperature anomalies, as generated by (and therefore cointegrating with) stochastic trends in radiative forcing components. On the other hand, recent contributions such as Estrada and Perron (2016) point to a common nonlinear deterministic trend in total radiative forcing and temperature anomalies, with significant breaks in slope in the 1960s and 1990s, and stationary fluctuations about trend. The latter structural breaks might be accounted by the contribution of natural variability oscillations such as the Atlantic Multidecadal Oscillation (AMO) for the Northern hemisphere and the Antarctic Oscillation

[1] See Cai et al. (2015b) for details on the disruptive effects of El Niño events occurred in 1982-1983 and 1997-1998.

[2] Yet, Douglas and Christy (2009) show that about 88% of the temperature anomaly over the period 1979-2007 would be accounted by ENSO (El Niño3.4 lagged 4 months) and volcano climate forcing. A connection between the North Atlantic Oscillation (NAO), the Arctic Oscillation (AO) and global warming has also bee investigated. See Cohen and Barlow (2005).

(AAO or SAM) for the Southern hemisphere. Recent evidence of deterministic trends and structural break in temperature anomalies are also provided by Gay et al. (2009) and Mills (2013). According to Gay et al. (2009) structural breaks should however be related to natural phenomena such as Earth orbit changes or changes in radiative forcing, as determined by solar irradiance and greenhouse gases concentrations.

More recently, the focus of the debate has shifted from the contribution of ENSO and other natural variability oscillations to global warming to the *implications of global warming for the frequency and amplitude of the ENSO and IOD phenomena*. As pointed out by Cai et al. (2015a,b; 2014) and Kim et al. (2014), while no consensus view has emerged to date, it is however expected that ENSO extremes will increase in amplitude and frequency and ENSO teleconnections will shift eastward, both as consequences of mean climate state changes. A sizable increase in the frequency of extreme positive Indian Ocean Dipole (pIOD) events might also be expected (Ng et al., 2015). See also Coumou and Rahmstorf (2012) on these issues.

In light of the above issues in this paper we further assess the linkages between temperature anomalies, radiative forcing and ENSO. The paper innovates the available literature in various directions. By testing for structural change and long memory, we find that temperature anomalies since the 1980s are best described by a short memory process about a single level shift occurring in the mid-/late 1990s. While the latter could in principle be related to concurrent very strong El Niño events or other natural variability oscillations (Estrada and Perron, 2009), we however find stronger evidence for its connection to radiative forcing, consistent with Gay et al. (2009). By means of a new flexible trend modeling approach, we uncover a nonlinear linkage between radiative forcing and global temperature anomalies. The nonlinear trend closely tracks the low frequency evolution in temperature anomalies, also accounting for the mid-end 1990s level switch, the 1998-2013 "warming hiatus" and the current steepening in trend temperatures. Therefore, consistent with Estrada and Perron (2016), our evidence is against the view of a recent slowdown in global warming; it is also against explanations that associate the hiatus to natural variability factors such as AMO, PDO, ENSO. Radiative forcing is also found to account for trend dynamics in SOI, therefore providing evidence that indeed global warming might affect natural variability oscillations such as ENSO, and therefore contribute to their disruptive effects (Cai et al., 2015a,b; 2014; and Kim et al., 2014).

In the paper we also document the feature of time-varying volatility of temperature anomalies. The feature is well described by a nonstationary generalized autoregressive conditional heteroskedastic process (IGARCH) and suggests the presence of alternating regimes in which periods of (relatively) unstable changes in temperature anomalies tend to be followed by periods in which changes are more dampened, and the other way around. The same feature is uncovered for SOI. In this respect, a sizable rise in SOI volatility can be noted since mid-2000s, concurrent with a somewhat earlier decrease in volatility for temperature anomalies and the steepening in the radiative forcing trend, consistent with feedback effects of global warming to ENSO fluctuations. The detected GARCH properties for temperature anomalies and SOI are then further assessed in the framework of a new dynamic conditional correlation model, i.e. the Semiparametric-DCC model (SP-DCC; Morana, 2015), which allows for the modeling of time-varying interlinkages across temperature series and in relation to ENSO. The proposed SP-DCC model is shown to compare favorably to exact ML and Engle (2002) DCC model in a Monte Carlo analysis.

We then document the presence of time-varying conditional correlations relating tem-

perature anomalies across various zones and SOI. In this respect we find a correlation pattern consistent with ENSO effects in the Tropics and its teleconnections. For instance, a negative conditional correlation is detected between SOI and the Tropics anomaly; hence, an El Niño (La Niña) event, yielding a negative (positive) SOI, would then lead to a warm (cool) phase in the Tropics. Moreover, we find a positive correlation between the Tropics anomaly and the Northern and Southern Extratropic anomalies, and between the Northern Extratropic and the Northern Polar anomalies, the Southern Extratropic and the Southern Polar anomalies. According to the latter correlation pattern, the warm (cool) phase started by an El Niño (La Niña) event in the Tropics, through the working of the "atmospheric bridge", would be then propagated to the Extratropics and Poles.

The rest of the paper is organized as follows. In Section 2 we introduce the temperature anomaly data and assess their persistence properties and connection with ENSO and radiative forcing. In Section 3 we introduce the semiparametric dynamic conditional correlation model (SP-DCC) and assess its small sample properties by means of Monte Carlo analysis. In Section 4 we then perform the conditional correlation analysis and further asses the interlinkages across temperature anomalies in various zones and ENSO. Finally, Section 5 concludes.

2 Persistence properties of anomalies

Our information set is monthly and spans the period 1978:12 through 2016:12, for a total of 457 observations. It consists of average land and ocean temperature anomalies for the entire globe (GL; 90S-90N) and seven zones, namely the Northern Hemisphere (NH; 0-90N), the Southern Hemisphere (SH; 90S-0), the Tropics (Trpcs; 20S-20N), the Northern Extratropic (NoExt; 20N-90N), the Southern Extratropic (SoExt; 90S-20S), the Northern Polar (NoPol; 60N-90N), the Southern Polar (SoPol; 90S-60S). The source is the NASA Goddard Institute for Space Studies and we refer to Christy et al. (2011) for details concerning data construction.[3] We also include the Southern Oscillation Index (SOI) to track the temporal evolution of ENSO episodes.[4]

Persistence properties of temperature anomalies have been subject to careful assessment in the literature. There are two main competing views, differing in terms of the statistical model employed to account for the warming trend detected in the data, rather than for its attribution to causing factors. In fact, while it is in general agreed that the warming trend is determined by radiative forcing, both of natural and anthropogenic origin, its stochastic or deterministic nature is contended. On the one hand, Kaufmann et al. (2013) and Schmith et al. (2012) point to a stochastic trend in global and Northern (NH) and Southern (SH) hemisphere temperature anomalies, as generated by (and therefore cointegrating with) stochastic trends in radiative forcing components.[5] Feed-

[3] http://www.nsstc.uah.edu/data/msu/v6.0/tlt/uahncdc_lt_6.0.txt

[4] The Southern Oscillation describes a bimodal variation in sea level barometric pressure between observation stations at Darwin, Australia and Tahiti. It is quantified in the Southern Oscillation Index (SOI), which is a standardized difference between the two barometric pressures. Normally, lower pressure over Darwin and higher pressure over Tahiti (La Niña conditions) encourages a circulation of air from east to west, drawing warm surface water westward and bringing precipitation to Australia and the western Pacific. When the pressure difference weakens (El Niño conditions) parts of the western Pacific, such as Australia experience severe drought, while across the ocean, heavy precipitation can bring flooding to the west coast of equatorial South America.

[5] Earlier evidence on integration and cointegration properties of temperature anomalies can be found in Stern and Kaufmann (2000), Kaufmann and Stern (2002), Kaufmann et al. (2006), Mills (2009).

back effects from temperature anomalies to radiative forcing have also been documented in this literature. For instance, Kaufmann et al. (2006) document a feedback loop in which temperature increases due to anthropogenic activities that emit greenhouse gases change flow to and from the atmosphere in a way that the radiative forcing of greenhouse gases is increased, generating a further increase in temperature. Schmith et al. (2012) also find that it is surface air temperature to adjust to the average temperature of the upper ocean, consistent with oceans' larger heating storage capacity. The latter finding is also consistent with the evidence of unidirectional Granger causality of temperature anomalies from SH to NH (Kaufmann and Stern, 2007; Harvey and Mills, 2001), due to the larger water content of SH relative to NH (and the different heating storage of water relative to land).

On the other hand, Estrada and Perron (2016) point to a common nonlinear deterministic trend in total radiative forcing and temperature anomalies, with significant breaks in slope in the 1960s and 1990s, and stationary fluctuations about trend. More precisely the first break is detected in 1962 and 1968 and the second break in 1989 and 1991, for NASA and HadCRUT4 data, respectively. This finding updates earlier evidence of trend stationarity and different timing in breaks for global and Northern and Southern hemispheres temperature anomalies, as reported by Gay et al. (2009) and Mills (2013)[6]. According to Estrada and Perron (2016), the latter feature would be accounted by the contribution of natural variability oscillations such as the Atlantic Multidecadal Oscillation (AMO) for the Northern hemisphere and the Antarctic Oscillation (AAO or SAM) for the Southern hemisphere. Moreover, even the recent slowdown in the warming trend, i.e. the hiatus, might be related to radiative forcing, i.e. mostly to CFC and methane reductions, rather than to natural variability factors such as AMO, PDO, ENSO, or lower solar activity, as claimed by Kosaka and Xie (2013). See also Pretis et al. (2015) on this issue. Estrada and Perron (2016) also update earlier evidence concerning persistence properties of temperature fluctuations about deterministic trends, which would be best described by a weakly stationary process. This contrasts with previous evidence of Bloomfield (1992) and Chung and Baillie (2002), pointing to stationary long memory fluctuations in global, NH and SH temperature anomalies about a linear deterministic trend. While long memory in temperature fluctuations might be an artifact due to a neglected slowly varying nonlinear trend function and/or alternating regimes/structural breaks as claimed by Mills (2007)[7], there also are valid reasons for this feature to be genuine, and related to effects of cross-sectional aggregation (Granger,1980) or the occurrence of shocks of stochastic magnitude and stochastic duration (Parke, 1999). In the current framework, the long memory phenomenon could be then easily associated with the cumulative effect of various radiative forcing mechanisms and/or to the contribution of natural variability

See also Chang et al. (2016) for recent evidence from nonstationarity analysis extended to the density function of temperature anomalies.

[6]The break points detected by Gay et al. (2009) are 1977, 1985, 1911 for global, NH and SH temperature anomalies, respectively. The break points are also associated wit Earth orbit changes, solar irradiance and greenhouse gases concentrations. Mills (2013) updates the latter estimates to 1964 for SH temeperature and 1976 for both global and NH temperatures. See also Bloomfield (1992) and Zheng and Basher (1999) for earlier evidence of determininistic trends in temperature anomalies. See also Mills (2006) for evidence of a more pronounced warming trend in NH temperatures since the 1970s, robust to stochastic of deterministic trend modeling.

[7]See Diebold and Inoue (2011) and references there in for a more general discussion on the difficuly of distinguishing deterministic nonstationarity and long memory. See also Rea et al. (2011) and Mann (2011) for recent views against the long memory feature.

oscillations, such as ENSO, particularly in their most extreme manifestations.[8]

In light of the contrasting results available in the literature in the paper we reassess the persistence properties of temperature anomalies for various zones and of SOI, by testing for stochastic nonstationarity versus trend stationarity/structural break, long memory versus short memory and genuine long memory versus spurious persistence generated by neglected structural change. We also asses the role of radiative forcing to in determining trend dynamics in temperature anomalies. The results of the persistence analysis are reported in Table 1, Panels A-D and Table 2, Panels A-B.

2.1 Testing for deterministic versus stochastic non stationarity

As shown in Panel A, the null of stochastic nonstationarity is rejected by the ADF test for all the temperature anomalies and the SOI index at the usual significance levels. The finding is robust to the deterministic specification used in the ADF regressions. This finding is against earlier evidence of a unit root in temperature anomalies generated by I(1) trends in radiative forcing components, as for instance reported in Stern and Kaufmann (2000), Kaufmann and Stern (2002), Kaufmann et al. (2006), Mills (2009).

In Panel B we also report the outcome of the Bai-Perron (1998) UD-max structural break tests. As shown by Laveille and Moulines (2000), despite not accounting for the feature directly, the Bai-Perron (1998) tests can yield some guidance also in the presence of long memory and might therefore be useful to distinguish spurious persistence due to neglected structural change from genuine long memory. Consistent with Estrada and Perron (2016) and Gay et al. (2009), the overall evidence point to a single break point since the 1980s, yet located about the mid-/end 1990s (1995 through 1998) for all the temperature anomalies series, rather than in 1991, similar to McKitrick and Vogelsang (2014). The detected break point might possibly be related to concurrent El Niño events (1995-1996 (weak); 1997-1998 (very strong)) and fading away of the cooling effect of the vulcanian eruption in the Philippines (Mt. Pinatubo in 1991).

The above evidence is clear-cut for the Northern zones, i.e. NH, NoExt and NoPol, and for SoPol, as the LWZ information criterion select a single break and the Bai-Perron SupF test does not allow to reject the null hypothesis of a single break against the alternative of two breaks. While a similar results is shown by the SupF test also for the other anomalies, LWZ however points to up to 3 breaks for GL, two breaks for Trpcs, SoExt and SOI and to two/four breaks for SH. The additional break points would be located in 2015 and in 1986 (not reported), and might be therefore related to the very strong 2015-2016 El Niño event and to the fading away of the cooling effect of the vulcanian eruption in Mexico (El Chichon in 1982).

2.1.1 Testing for breaks versus long memory

Since structural change and/or long memory could account for temperature anomalies persistence, but they are not easily distinguishable with the available tests (Diebold and Inoue, 2001), in Panel C we report selected results for the estimation of four different long memory models. The models are a "pure" ARFIMA(p,d,q) model (Model 1), an "augmented" ARFIMA(p,d,q) model with a single level switch selected according to the

[8] Pellettier and Turcotte (1997) also provides a theoretical explanation for the presence of long memory in temperature anomalies based on an advection-diffusion model of the vertical transport of heat and water vapor in the atmosphere.

Bai-Perron UD-max test (Model 2), an ARFIMA(p,d,q) model augmented with a linear time trend (Model 3) and an ARFIMA(p,d,q) model with both switching intercept and linear time trend (Model 4). Hence, the estimated models are

$$\phi(L)(1-L)^d y_t = c_t + \theta(L)\varepsilon_t \quad \varepsilon_t \sim NID\left(0,\sigma^2\right) \tag{1}$$

where

$$\begin{aligned} c_t &= c_0 && \text{in Model 1} \\ c_t &= c_0 + c_1 I_{bp} && \text{in Model 2} \\ c_t &= c_0 + c_2 t && \text{in Model 3} \\ c_t &= c_0 + c_1 I_{bp} + c_2 t && \text{in Model 4} \end{aligned}$$

where I_{bp} is a step indicator function, taking unitary value from the estimated break point onwards and zero value otherwise; $\phi(L) = 1 - \sum_{i=1}^{p} \phi_i L^i$ and $\theta(L) = 1 + \sum_{i=1}^{q} \theta_i L^i$ are stationary polynomials in the lag operator of order p and q, respectively.

By jointly assessing structural change and long memory, more robust results are then expected concerning persistence properties. ML estimates of the above models are reported in Panel C. As shown in Panel C, there is evidence of long memory for all the anomalies series, independently of the deterministic parameterization, also fairly stable across specifications. A pure long memory model, i.e. with $p = q = 0$, yields white noise residuals for all the anomaly series according to standard misspecification tests (not reported).[9]

In particular, evidence of nonstationary long memory ($d > 0.5$) is found for GL, NH, SH, Trpcs and SOI, while for NoExt, SoExt, NoPol and SoPol the evidence point to stationary long memory ($0 < d < 0.5$). As an implication, temperature anomaly shocks would dissipate over time, yet anomalies might not be mean reverting. According to figures, persistence is strongest at the Tropics ($d = 0.90$) and weakest for NoPol ($d = 0.28$) and SoPol ($d = 0.26$); intermediate values are found for NoExt ($d = 0.48$) and SoExt ($d = 0.38$). Non stationary long memory is detected when averaging across zones to yield NH and SH ($d = 0.60$) and GL ($d = 0.65$) temperature anomalies.

Concerning the deterministic specification, according to the BIC information criterion the pure long memory model (Model 1) is selected in five out of eight cases (GL, NH, SH, Trpcs, SoPol) and for SOI, i.e. for the nonstationary long memory cases (apart from SoPol); the long memory model augmented with a linear time trend (Model 3) is selected in two cases (SoExt and NoPol); the long memory model augmented with a one-off switch (Model 2) in level is selected only in one case (NoExt). Moreover, in none of the cases the model augmented with both the linear time trend and the step dummy (Model 4) is selected by either the BIC or the AIC criteria, confirming previous evidence of McKitrick and Vogelsang (2014) that the two deterministic specifications can be held as substitute rather than complementary.[10]

[9] Details are available upon request from the authors.

[10] McKitrick and Vogelsang (2014) estimate a level shift in 1997:12 for GL; once allowing for the level shift, the null of no linear trend cannot be any longer rejected over the period 1958-2012.

2.1.2 Testing for long memory versus short memory and breaks

Since no short memory (AR or MA) component is selected in the long memory models reported in Panel C, we reassess persistence properties of temperature anomalies holding short and long memory as substitute rather than complementary properties. Hence, a short memory version ($d = 0$) of Models 1 through 4 above are estimated by ML. The estimates are reported in Panel D. As shown in Panel D, according to information criteria, a short memory autoregressive model is preferred to its corresponding long memory model for all the anomalies, performing similarly well in terms of misspecification tests (not reported).[11] In all cases a parsimonious AR(2) model is selected according to a general to specific model selection strategy, apart from Trpcs and SoPol (AR(1)) and SOI (AR(3)). Moreover, according to information criteria, the AR model with switching intercept (Model 2) is selected as best model for all the temperature series, apart from SoPol. For the latter series and for SOI also a constant mean AR model (Model 1) is selected by the BIC. As shown in the Table, the estimated persistence parameter ($\sum_{i=1}^{p} \phi_i$) for GL is about 0.8, consistent with similar estimates obtained for NH and SH. Similar to what found for the long memory models, persistence of temperature shocks is highest at the Tropics (0.90) and lowest at the Poles (0.30), showing a similar intermediate value for NoExt and SoExt (0.5-0.6).

2.1.3 Flessible modeling of structural change

In light of the evidence of short memory plus structural change in temperature anomalies and SOI, following Baillie and Morana (2012) we implement an Adaptive-AR model. The Adaptive-AR model is

$$\phi(L) y_t = c_t + \varepsilon_t \qquad \varepsilon_t \sim NID\left(0, \sigma^2\right) \tag{2}$$

where the deterministic function follows a Gallant (1981) flexible functional form

$$c_t = c_0 + c_1 t + \sum_{i=1}^{p} \gamma_i \sin(2\pi i t/T) + \sum_{i=1}^{p} \delta_i \cos(2\pi i t/T) \qquad p = 1, ..., 5 \tag{3}$$

The Adaptive-AR model has the advantage of allowing for a more flexible modeling of structural change, given the ability of the Gallant (1981) flexible functional form to approximate a very general class of nonlinear functions (see Becker et al., 2006; Enders and Lee, 2012; Baillie and Morana, 2009, 2012; Perron et al., 2016). This is particularly relevant for the current application given the non univocal determination of the break point across temperature anomalies and even the finding of no breaks for SoPol and SOI. The latter deterministic specification has also been recently employed by Estrada and Perron (2016) for modeling the trend in temperature anomalies.

In Table 2, Panel A we report results of the Perron et al. (2016) Wald test for the presence of a nonlinear temporal trend approximated by the Gallant trigonometric expansion, which is valid under the assumption of both I(0) and I(1) disturbances. The test has the usual chi-square or standard Normal distribution under the null hypothesis of no deterministic nonlinearity. As shown in Panel A, consistent with the results of the persistence analysis, the test rejects the null of no-nonlinearity for all the series, apart

[11] Details are available upon request from the authors.

from Trpcs and SOI, when the linear deterministic trend is omitted from the specification (3); on the other hand, weaker evidence of deterministic nonlinearity is detected once the linear trend is included in the specification.

In Table 2, Panel B we then report the Adaptive-AR models, estimated by ML, where the deterministic specification has been selected following a general to specific strategy. Consistent with the results of the Wald test analysis, only low order components are found to be statistically significant. In particular a first order sine expansion appears to be appropriate for all temperature anomalies apart from SoPol. However, according to the BIC information criteria, the estimated Adaptive-AR models reported in Panel B (Table 2) never perform better than the standard AR model with switching intercept reported in Panel D (Table 1). This is somewhat in contrast with Estrada and Perron (2016), where the nonlinear deterministic trend is found to be successfully approximated by the Gallant flexible functional form, albeit on a much larger sample of annual data than the one considered in this study.

2.2 Radiative forcing and breaks in temperature anomalies

Earlier evidence on structural breaks in temperature anomalies relate them to the contribution of natural variability oscillations such as the Atlantic Multidecadal Oscillation (AMO) for the Northern hemisphere and the Antarctic Oscillation (AAO or SAM) for the Southern hemisphere (Estrada and Perron, 2016), or to other natural or human made phenomena, such as Earth orbit changes, solar irradiance and greenhouse gases concentrations (Gay et al., 2007). In light of the robust evidence of a structural breaks affecting temperature anomalies, we have then assessed their possible connection with radiative forcing (RF). This is consistent with Estrada and Perron (2016) where the deterministic nonlinear trend in temperature anomalies is found to be determined by the nonlinear deterministic trend in radiative forcing.

However, our analysis differs from Estrada and Perron (2016) as it is conducted in the more comprehensive framework of an Adaptive-X-AR-GARCH model

$$\begin{aligned} \phi(L)\, y_t &= c_t + h_t^{1/2} v_t \qquad v_t \sim NID(0,1) && (4) \\ h_t &= \beta h_{t-1} + \alpha \varepsilon_{t-1}^2 && (5) \end{aligned}$$

where $\alpha = 1 - \beta$, $\varepsilon_t = h_t^{1/2} v_t$.

Different models are considered, according to the specification of the deterministic component c_t. The latter is specified as

$$c_t = c_0 + c_1 I_t \tag{6}$$

for the pure structural break model (AR-B), where I_t is a step dummy variables with unitary values set according to the Bai-Perron structural break tests;

$$c_t = c_0 + c_2 RF_t + \sum_{i=1}^{p} \gamma_i \sin(2\pi i RF_t^*) + \sum_{i=1}^{p} \delta_i \cos(2\pi i RF_t^*) \qquad p = 1, ..., 5 \tag{7}$$

for the Adaptive-X-AR model, where RF_t^* is RF_t scaled to range between 0 and 1;

$$c_t = c_0 + c_1 I_t + c_2 RF_t + \sum_{i=1}^{p} \gamma_i \sin(2\pi i RF_t^*) + \sum_{i=1}^{p} \delta_i \cos(2\pi i RF_t^*) \qquad p = 1, ..., 5 \tag{8}$$

for the hybrid Adaptive-X-AR-B model, which nests the former two models.

In all cases we also model the conditional variance function; as it will be shown below, temperature anomalies and SOI series are characterized by volatility clusters. Possibly due noisiness, the latter property is not immediately apparent and might go fully neglected when standard misspecification tests are employed. Below we show that models that allow for the IGARCH components are systematically preferred to their constant conditional variance version by information criteria.

2.2.1 Forecasting and monthly interpolation of radiative forcing data

As radiative forcing data are available at the annual frequency and up to 2011 only, implementation of the Adaptive-X-AR and Adaptive-X-AR-B models requires forecasting of radiative forcing data through 2016 and monthly interpolation. Concerning sample extension, naive forecasts over the period 2012 through 2016 have been generated by means of structural time series models specified for each of the various radiative forcing components; forecasts for total radiative forcing are then computed by aggregating the forecasts for the various components. Following Hansen et al. (2005), radiative forcing has been decomposed in various categories, i.e., Well-Mixed Greenhouse Gases (WMGG; carbon dioxide (CO_2), methane (NH4), nitrous oxide (N2O) and chlorofluorocarbons (CFCs)), Ozone (O3), Stratospheric Water Vapor (StrH2O), Reflective Tropospheric Aerosols (ReflAer), Tropospheric Aerosol Indirect Effects (AIE), Black Carbon Aerosols (BC), Snow Albedo (snowAlb), Stratospheric Aerosols (StrAer), Solar Irradiance (Solar), Land Use (including irrigation; LandUse).[12] As we are interested in the modeling of the trend in radiative forcing, the Stratospheric Aerosols (StrAer) component is omitted. The latter series, over the sample of interest, is heavily influenced by the major volcanic eruptions occurred in 1991 in the Philippines (Mt. Pitanubo) and in 1982 in Mexico (El Chichon), which lead to a sizable, temporary temperature "cooling" around the globe.

Monthly radiative forcing series are obtained by means of nonlinear interpolation of annual figures. In practice a monthly step function is firstly constructed by holding constant the annual radiative forcing figures across the corresponding twelve months. Then, the step function series is regressed on the Gallant specification in (3) by OLS. The fitted process RF_t yields the interpolated monthly radiative forcing series which is employed in the rest of the analysis.

Actual and forecast annual figures for radiative forcing components over the period 1978-2016, and the interpolated monthly figures are reported in Figure 1.[13] As shown in the Figures, naive forecasts point to radiative forcing increasing through 2016, yet at slower pace; hence, the scenario might be considered conservative, potentially avoiding an upper bias in the estimated contribution of radiative forcing to global warming over the forecasted period. Moreover, the nonlinearly interpolated series track very closely the trend evolution of the annual radiative forcing series, supporting its use in the rest of the analysis.

2.2.2 Estimation results

ML estimates of the various models are reported in Table 3, Panel A (AR-B), Panel B (Adaptive-X-AR) and C (Adaptive-X-AR-B). As shown in Table 3, all models are

[12] The data ara available at https://data.giss.nasa.gov/modelforce/Fe_H11_1880-2011.txt

[13] Details are available upon request from the authors.

equivalent concerning residual properties and fit, as in none of the cases evidence of misspecification is detected by standard diagnostics. Moreover, according to the coefficient of determination, the explanatory power of the various models is similarly sizable, particularly for the aggregate series, i.e. about 0.70 for GL, NH and SH and 0.80 for Trpcs; less sizable for the Poles, i.e. 0.30 and 0.10 for NoPol and SoPol, respectively; intermediate, i.e. 0.40 to 0.60, for NoExt, SoExt and SOI.

However, models can be ordered on the basis of information criteria. In this respect, apart from SoPol, for which no deterministic component is detected, the findings point to a clear-cut linkage between temperature anomaly break processes and radiative forcing. In fact, according to the AIC and BIC criteria, Adaptive-X-AR models (Panel B) are superior to AR-B models (Panel A) for NoExt, SoExt, NoPol and SOI. Similar conclusions can be drawn for the aggregate anomalies GL, NH, SH and Trpcs, yet according to AIC criterion only. Moreover, according to the BIC criterion Adaptive-X-AR models (Panel B) are superior also to the hybrid Adaptive-X-AR-B models (Panel C) for NoExt, SoExt, NoPol and SOI. Moreover, for GL, NH, SH the hybrid models perform best according to the AIC and BIC criteria, while for Trpcs the hybrid model performs best according to the AIC criterion only. For the latter models the radiative forcing variable becomes statistically insignificant once the break process is added to the specifications, albeit some of its Fourier components are retained in the specification.

Concerning the specification selected for SOI, the statistical significance of the radiative forcing variable might suggest a feedback effect from global warming to ENSO. This is consistent with current expectations that ENSO and other natural oscillators might increase in amplitude and frequency and their teleconnections might be shifted, both as consequences of mean climate state changes (Cai et al.. 2015a,b; 2014; Kim et al., 2014; Ng et al., 2015; Coumou and Rahmstorf, 2012). Our findings are supportive of the above arguments, as the negative sign of the estimated coefficient of the radiative forcing variable points to global warming (cooling) enhancing El Niño (La Niña) events. Interestingly, the linkage between radiative forcing and ENSO appears to be highly nonlinear and similar to what detected for Trpcs, the geographical zone which is most closely and directly affected by ENSO.

Finally, while no evidence of misspecification is detected for the homoskedastic version of the Adaptive-AR models (not reported), allowing for IGARCH effects in conditional variance always leads to a better performing model according to the BIC criterion and often also according to the AIC criterion (see Table 3, *AIC* and *BIC Homosk* versus AIC and BIC for the conditionally heteroskedastic models). This is consistent with the presence of a hidden dynamic structure in second moments which might remain undetected due to the large and dominating observational noise component.

Temperature anomalies and the nonlinear trend determined by radiative forcing are shown in Figure 2, while the estimated conditional variance functions are plotted in Figure 3. As shown in Figure 2, a level switch, occurring near mid-/end 1990s can be noted across all the anomalies series, apart from SoPol and SOI. Moreover, a different degree of persistence is shown by the various anomalies, i.e. strongest for GL, NH and Trpcs and weakest for NoPol and SoPol. The latter anomalies also seem to show a larger noise components, similar to SH and SoExt relative to NH and NoExt. All these feature seems to be adequately described by the selected Adaptive-X-AR-IGARCH(1,1) model. In particular, the radiative forcing nonlinear trend closely tracks the low frequency evolution in temperature anomalies, also accounting for the mid-end 1990s level switch. According to the findings, radiative forcing is not only currently contributing to global

warming, but it also accounts for the 1998-2013 temperature hiatus. This is consistent with Estrada and Perron (2016), who also relate the hiatus to radiative forcing, i.e. to CFC and methane reductions, rather than to natural variability factors such as AMO, PDO, ENSO, or lower solar activity, as claimed by Kosaka and Xie (2013). See also Pretis et al. (2015) on this issue. Therefore, our evidence is against the thesis of a recent slowdown in global warming.

As shown in Figure 3, temperature anomaly series show clusters of more and less volatile periods, which alternate over time. A sizable rise in SOI volatility can be noted since mid-2000s, concurrent with a somewhat earlier decrease in volatility for global temperature (GL) and, in particular in the Southern Hemisphere, i.e. for Trpcs, SoExt, SoPol and SH overall, and for NoPol also. This finding is interesting and surely deserves further study, particularly in connection with the concurrent steepening in the radiative forcing trend shown in Figure 1. The detected GARCH properties for temperature anomalies and SOI/ENSO also invite a further assessment of their linkage, which we carry out below in the framework of a new dynamic conditional correlation model, i.e. the Semiparametric-DCC model (SP-DCC; Morana, 2015).

3 SP-DCC estimation of conditional correlations

The semiparametric dynamic conditional correlation model (SP-DCC; Morana, 2015) is defined by the following equations

$$\mathbf{y}_t = \boldsymbol{\mu}_t(\boldsymbol{\delta}) + \boldsymbol{\varepsilon}_t \tag{9}$$

$$\boldsymbol{\varepsilon}_t = \mathbf{H}_t^{1/2}(\boldsymbol{\delta})\mathbf{z}_t \tag{10}$$

where $\mathbf{y}_t$ is the $N \times 1$ column vector of the variables of interest, $\boldsymbol{\mu}_t(\boldsymbol{\delta})$ is the $N \times 1$ conditional mean vector $E(\mathbf{y}_t|I_{t-1})$, $\boldsymbol{\delta}$ is a vector of parameters, I_{t-1} is the sigma field; $\mathbf{H}_t(\boldsymbol{\delta})$ is the $N \times N$ conditional variance-covariance matrix $Var(\mathbf{y}_t|I_{t-1})$. Moreover, the random vector $\mathbf{z}_t$ is of dimension $N \times 1$ and assumed to be *i.i.d.* with first two moments $E(\mathbf{z}_t) = \mathbf{0}$ and $Var(\mathbf{z}_t) = \mathbf{I}_N$. Concerning the specification of the conditional variance-covariance matrix $\mathbf{H}_t(\boldsymbol{\delta})$, we assume that the elements along its main diagonal, i.e., the conditional variances $Var(y_{i,t}|I_{t-1}) \equiv h_{i,t}$ follow a GARCH(1,1) process

$$h_{i,t} = \omega_i + \alpha_i \varepsilon_{i,t-1}^2 + \beta_i h_{i,t-1} \qquad i = 1, ..., N \tag{11}$$

subject to the usual restrictions to ensure that the conditional variances are positive almost surely at any point in time.

Concerning the definition of the conditional covariances, a nonparametric specification is posited, grounded on the *polarization* identity

$$Cov(A, B) \equiv \frac{1}{4}\left[Var(A + B) - Var(A - B)\right] \tag{12}$$

given that $Var(A \pm B) = Var(A) + Var(B) \pm 2Cov(A, B)$, for any two random variables A and B.

Accordingly, the off-diagonal elements of $\mathbf{H}_t$, $Cov(y_{i,t}, y_{j,t}|I_{t-1}) \equiv h_{ij,t}$, are

$$h_{ij,t} = \frac{1}{4}\left[Var_{t-1}(y_{i,t} + y_{j,t}) - Var_{t-1}(y_{i,t} - y_{j,t})\right] \qquad i, j = 1, ..., N \qquad i \neq j. \tag{13}$$

By defining the aggregate variables $y^+_{ij,t} \equiv y_{i,t} + y_{j,t}$ and $y^-_{ij,t} \equiv y_{i,t} - y_{j,t}$, and assuming a GARCH(1,1) specification for their conditional variance processes $Var_{t-1}(y^+_{ij,t}|I_{t-1}) \equiv h^+_{ij,t}$ and $Var_{t-1}(y^-_{ij,t}|I_{t-1}) \equiv h^-_{ij,t}$ as well, we then have

$$h^+_{ij,t} = \omega^+_{ij} + \alpha^+_{ij}\varepsilon^{+2}_{ij,t-1} + \beta^+_{ij}h^+_{ij,t-1} \qquad i,j = 1,...,N \qquad i \neq j \tag{14}$$

$$h^-_{ij,t} = \omega^-_{ij} + \alpha^-_{ij}\varepsilon^{-2}_{ij,t-1} + \beta^-_{ij}h^-_{ij,t-1} \qquad i,j = 1,...,N \qquad i \neq j \tag{15}$$

where $\varepsilon^+_{ij,t} = \varepsilon_{i,t} + \varepsilon_{j,t}$ and $\varepsilon^-_{ij,t} = \varepsilon_{i,t} - \varepsilon_{j,t}$.

3.1 Estimation of the SP-DCC model

Consistent and asymptotically Normal estimation is obtained by QML, following a two-step procedure similar to Engle (2002). Consider the Gaussian log-likelihood for the model in (10)

$$L = -\frac{1}{2}\sum_{t=1}^{T}\left(N\log(2\pi) + \log|\mathbf{H}_t| + \boldsymbol{\varepsilon}'_t\mathbf{H}_t^{-1}\boldsymbol{\varepsilon}_t\right). \tag{16}$$

Following Engle (2002), the latter can be written as

$$L = -\frac{1}{2}\sum_{t=1}^{T}\left(N\log(2\pi) + 2\log|\mathbf{D}_t| + \boldsymbol{\varepsilon}'_t\mathbf{D}_t^{-1}\mathbf{D}_t^{-1}\boldsymbol{\varepsilon}_t) + (-\boldsymbol{\varepsilon}'_t\boldsymbol{\varepsilon}_t + \log|\mathbf{R}_t| + \boldsymbol{\varepsilon}'_t\mathbf{R}_t^{-1}\boldsymbol{\varepsilon}_t\right) \tag{17}$$

where

$$\mathbf{D}_t = diag\left(h_{1,t}^{1/2},...,h_{N,t}^{1/2}\right)$$

and the conditional correlation matrix $\mathbf{R}_t$ is defined as

$$\mathbf{R}_t = \mathbf{D}_t^{-1}\mathbf{H}_t\mathbf{D}_t^{-1}.$$

The log-likelihood function in (17) is the sum of a *volatility part*

$$L_v(\boldsymbol{\theta}) = -\frac{1}{2}\sum_{t=1}^{T}\left(N\log(2\pi) + 2\log|\mathbf{D}_t| + \boldsymbol{\varepsilon}'_t\mathbf{D}_t^{-1}\mathbf{D}_t^{-1}\boldsymbol{\varepsilon}_t\right) \tag{18}$$

and a *correlation part*

$$L_C(\boldsymbol{\theta},\boldsymbol{\phi}) = -\frac{1}{2}\sum_{t=1}^{T}\left(-\boldsymbol{\varepsilon}'_t\boldsymbol{\varepsilon}_t + \log|\mathbf{R}_t| + \boldsymbol{\varepsilon}'_t\mathbf{R}_t^{-1}\boldsymbol{\varepsilon}_t\right). \tag{19}$$

The volatility part in (18) is the sum of individual GARCH likelihoods

$$L_v(\boldsymbol{\theta}) = -\frac{1}{2}\sum_{t=1}^{T}\sum_{i=1}^{N}\log(2\pi) + \log h_{i,t} + \frac{\varepsilon^2_{i,t}}{h_{i,t}} \tag{20}$$

which is then jointly maximized by separately maximizing each term. The conditional variances $h_{i,t}$, $i = 1,...,N$, i.e. the elements along the main diagonal of $\mathbf{H}_t$, are therefore estimated equation by equation by means of QML, using the conditional mean residuals $\varepsilon_{i,t}$, $i = 1,...,N$.

Differently from DCC, SP-DCC does not maximize the correlation part in (19) directly, but rather the sum of individual GARCH likelihoods for the aggregate series $y^+_{ij,t}$ and $y^-_{ij,t}$, i.e.

$$\begin{aligned} L_{SP}(\boldsymbol{\phi}) &= -\frac{1}{2}\sum_{t=1}^{T} 2 \sum_{i=1}^{N}\sum_{j>i}^{N}\left(\log(2\pi) + \log h^+_{ij,t} + \frac{\varepsilon^{+2}_{ij,t}}{h^+_{ij,t}}\right) \\ &\quad -\frac{1}{2}\sum_{t=1}^{T} 2 \sum_{i=1}^{N}\sum_{j>i}^{N}\left(\log(2\pi) + \log h^-_{ij,t} + \frac{\varepsilon^{-2}_{ij,t}}{h^-_{ij,t}}\right) \end{aligned} \tag{21}$$

which is jointly maximized by separately maximizing each term. Hence, the conditional variances for the aggregates $h^+_{ij,t}$, $h^-_{ij,t}$, $i,j = 1,...,N$, $i \neq j$, are estimated equation by equation by means of QML, using the aggregated conditional mean residuals $\varepsilon^+_{ij,t} = \varepsilon_{i,t} + \varepsilon_{j,t}$ and $\varepsilon^-_{ij,t} = \varepsilon_{i,t} - \varepsilon_{j,t}$.

Through the polarization identity the conditional covariances are then computed, i.e. the off-diagonal elements of $\mathbf{H}_t$, $h_{ij,t}$, $i,j = 1,...,N$, $i \neq j$, are estimated nonparametrically by computing

$$\hat{h}_{ij,t} = \frac{1}{4}\left[\hat{h}^+_{ij,t} - \hat{h}^-_{ij,t}\right] \qquad i,j = 1,...,N \qquad i \neq j. \tag{22}$$

The conditional correlation matrix $\mathbf{R}_t$ is then estimated as

$$\hat{\mathbf{R}}_t = \hat{\mathbf{D}}_t^{-1}\hat{\mathbf{H}}_t\hat{\mathbf{D}}_t^{-1} \tag{23}$$

where

$$\hat{\mathbf{D}}_t = diag\left(\hat{h}^{1/2}_{1,t},...,\hat{h}^{1/2}_{N,t}\right) \tag{24}$$

and the correlation part in (19) can be evaluated provided $\hat{\mathbf{R}}_t$ is positive definite at each point in time (see Morana (2015) and below for the correction to be applied in the case of a non positive definite correlation matrix). Hence the proposed two-step approach to maximize the log-likelihood function is to find

$$\hat{\boldsymbol{\theta}} = \arg\max\left\{L_v(\boldsymbol{\theta})\right\} \tag{25}$$

$$\hat{\boldsymbol{\phi}} = \arg\max\left\{L_{SP}(\boldsymbol{\phi})\right\} \tag{26}$$

and then use these values to evaluate $L_C(\boldsymbol{\theta},\boldsymbol{\phi})$.

Then, under standard regularity conditions, the asymptotic distribution of the QML estimator is

$$T^{1/2}\left(\hat{\boldsymbol{\vartheta}} - \boldsymbol{\vartheta}_0\right) \rightarrow N\{\mathbf{0}, \mathbf{A}(\boldsymbol{\vartheta}_0)^{-1}\mathbf{B}(\boldsymbol{\vartheta}_0)\mathbf{A}(\boldsymbol{\vartheta}_0)^{-1}\} \tag{27}$$

where $\boldsymbol{\vartheta}_0 = \boldsymbol{\theta}_0, \boldsymbol{\phi}_0$ denotes the true value of the vector of parameters, $\mathbf{A}(\boldsymbol{\vartheta}_0)$ is the Hessian and $\mathbf{B}(\boldsymbol{\vartheta}_0)$ is the outer product gradient evaluated at the true parameter values. In fact, while the procedure does not maximize the joint log-likelihood in (17), consistent and asymptotically Normal estimation is however granted by the QML principle, under the standard assumptions.

3.2 Ex-post correction for well-behaved conditional covariance and correlation matrices

The ex-post correction to grant that $\hat{\mathbf{R}}_t$ is positive definite at each point in time can be implemented as follows. Firstly, if required, the estimated conditional correlations in $\hat{\mathbf{R}}_t$, $\hat{\rho}_{ij,t}$, $i \neq j$, are bounded to lie within the range $-1 \leq \hat{\rho}_{ij,t} \leq 1$ by applying the sign-preserving bounding transformation

$$\hat{\rho}^*_{ij,t} = \hat{\rho}_{ij,t}(1 + \hat{\rho}^k_{ij,t})^{-1/k} \tag{28}$$

where $k > 0$ and even, is selected optimally by minimizing the sum of squared Frobenious norms over the temporal sample

$$\arg\min_k \sum_{t=1}^{T} \left\| \hat{R}_t - \hat{R}^*_t \right\|^2_F = \arg\min_k \sum_{t=1}^{T} \sum_{i=1}^{N} \sum_{j=1}^{N} \left| \hat{\rho}_{ij,t} - \hat{\rho}^*_{ij,t} \right|^2 . \tag{29}$$

This yields $\hat{\mathbf{R}}^*_t$, the transformed correlation matrix, which satisfies, by construction, the Cauchy-Schwarz inequality.

Secondly, if required, positive definiteness is enforced by means of nonlinear shrinkage of the negative eigenvalues of the $\hat{\mathbf{R}}^*_t$ matrix toward their corresponding positive average values over the temporal sequence in which they are positive.[14] In practice, the eigenvalue-eigenvector decomposition of the transformed conditional correlation matrix $\hat{\mathbf{R}}^*_t$ is performed, yielding

$$\hat{\mathbf{R}}^*_t = \hat{\mathbf{E}}_t \hat{\mathbf{V}}_t \hat{\mathbf{E}}'_t$$

where $\hat{\mathbf{V}}_t$ is the diagonal matrix containing the ordered original (positive and negative) eigenvalues along the main diagonal and $\hat{\mathbf{E}}_t$ is the matrix containing the associated orthogonal eigenvectors. By denoting $\hat{\mathbf{V}}^*_t$ the diagonal matrix containing the ordered original and shrank positive eigenvalues, the new estimate of the conditional correlation matrix can be computed as

$$\hat{\mathbf{R}}^{**}_t = \hat{\mathbf{E}}_t \hat{\mathbf{V}}^*_t \hat{\mathbf{E}}'_t \tag{30}$$

which, by construction, is well-behaved at each point in time. The implied, well-behaved conditional covariance process at time period t is then

$$\hat{\mathbf{H}}^{**}_t = \hat{\mathbf{D}}_t \hat{\mathbf{R}}^{**}_t \hat{\mathbf{D}}_t$$

which obeys the Cauchy-Schwarz inequality and the positive definiteness condition, at each point in time, by construction. Other procedure can also be foreseen, a s for instance as treating the negative/zero eigenvalues as missing observations to be interpolated using the Kalman filter.

3.3 Small sample performance of the semiparametric estimator

This section explores the performance of semiparametric estimation of DCC models (SP) together with other standard estimation methods. In the simulation we make use of

[14] In the case the negative eigenvalues were negative over the whole temporal sequence, following Ledoit and Wolf (2012), any suitable small positive value can be used. Alternatively, extrapolation using a decay structure can be performed. For instance, based on the Marchenko-Pastur limiting distribution of the eigenvalues of a random covariance matrix filled with independent standard normal random values, a quadratic decay for eigenspectrum could be selected.

three different multivariate GARCH frameworks. The first considered framework is the Diagonal VECH as in Bollerslev et al. (1988). This framework allows to show the conditions needed for the use of the SP estimator.

Consider the following bivariate GARCH(1,1) model

$$\begin{bmatrix} y_{1t} \\ y_{2t} \end{bmatrix} = H_t^{\frac{1}{2}} \begin{bmatrix} z_{1t} \\ z_{2t} \end{bmatrix} \qquad \begin{bmatrix} z_{1t} \\ z_{2t} \end{bmatrix} \sim i.i.dN(0, I_2) \tag{31}$$

where

$$H_t = \begin{bmatrix} h_{1t} & h_{12t} \\ h_{12t} & h_{2t} \end{bmatrix} \tag{32}$$

The conditional covariance matrix follows the following bivariate system

$$\begin{aligned} \begin{bmatrix} h_{1t} & h_{12t} \\ h_{12t} & h_{2t} \end{bmatrix} &= \begin{bmatrix} \omega_1 & \omega_2 \\ \omega_2 & \omega_3 \end{bmatrix} + \begin{bmatrix} \beta_1 & \beta_2 \\ \beta_2 & \beta_3 \end{bmatrix} \begin{bmatrix} h_{1t-1} & h_{12t-1} \\ h_{12t-1} & h_{2t-1} \end{bmatrix} \\ &+ \begin{bmatrix} \alpha_1 & \alpha_2 \\ \alpha_2 & \alpha_3 \end{bmatrix} \begin{bmatrix} y_{1t-1}^2 & y_{1t-1}y_{2t-1} \\ y_{1t-1}y_{2t-1} & y_{2t-1}^2 \end{bmatrix} \end{aligned} \tag{33}$$

That is, in its VECH form

$$\begin{bmatrix} h_{1t} \\ h_{12t} \\ h_{2t} \end{bmatrix} = \begin{bmatrix} \psi_1 \\ \psi_2 \\ \psi_3 \end{bmatrix} + \begin{bmatrix} \beta_1 & 0 & 0 \\ 0 & \beta_2 & 0 \\ 0 & 0 & \beta_3 \end{bmatrix} \begin{bmatrix} h_{1t-1} \\ h_{12t-1} \\ h_{2t-1} \end{bmatrix} + \begin{bmatrix} \alpha_1 & 0 & 0 \\ 0 & \alpha_2 & 0 \\ 0 & 0 & \alpha_3 \end{bmatrix} \begin{bmatrix} y_{1t}^2 \\ y_{1t}y_{2t} \\ y_{2t}^2 \end{bmatrix} \tag{34a}$$

As already shown by Bollerslev et al. (1988), it is possible to substitute $h_{it} = y_{it}^2 - \eta_{it}$ into (32) in order to obtain the following VARMA representation for the squared returns

$$\begin{aligned} &\begin{bmatrix} (1-(\alpha_1+\beta_1)L) & 0 & 0 \\ 0 & (1-(\alpha_2+\beta_2)L) & 0 \\ 0 & 0 & (1-(\alpha_3+\beta_3)L) \end{bmatrix} \begin{bmatrix} y_{1t}^2 \\ y_{1t}y_{2t} \\ y_{2t}^2 \end{bmatrix} = \\ &= \begin{bmatrix} \psi_1 \\ \psi_2 \\ \psi_3 \end{bmatrix} + \begin{bmatrix} (1-\beta_1 L) & 0 & 0 \\ 0 & (1-\beta_2 L) & 0 \\ 0 & 0 & (1-\beta_3 L) \end{bmatrix} \begin{bmatrix} \eta_{1t} \\ \eta_{2t} \\ \eta_{3t} \end{bmatrix} \end{aligned} \tag{35}$$

where:

$$E\eta_{it}^2 = E(z_{it}^2 - 1)^2 Eh_{it}^2 = \frac{(\kappa_i - 1)h_i^2 \left\{1 - (\beta_i + \alpha_i)^2\right\}}{(1 - \beta_i^2 - 2\alpha_i\beta_i - \alpha_i^2\kappa_i)}$$

The contemporaneous aggregation of model (35) leads to an ARMA(3,3) unless we observe that, for some i and j, $(\alpha_i + \beta_i) = (\alpha_j + \beta_j)$, i.e. unless we have the case of root cancellation. For example, when $(\alpha_1 + \beta_1) = (\alpha_2 + \beta_2)$ then the contemporaneous aggregation of model (35) leads to an ARMA(2,2). In addition, when $(\alpha_1 + \beta_1) = (\alpha_2 + \beta_2) = (\alpha_3 + \beta_3)$ then the aggregate process for the squared return is an ARMA(1,1), with the conditional (co)variance being a GARCH(1,1) process. Similar findings hold for other combinations of (35) such as the difference process as considered by the SP estimator. Therefore, although the SP estimator represents an approximation for this framework, when the case of root cancellation arises this approximation gets more accurate. This seems to be the message from the following Monte Carlo simulation.

We generated model (31)-(32) using the following three parameters structures

$$
\begin{aligned}
&MODEL(i)\ for\ i = 1,2,3 \\
&\boldsymbol{\omega}_i = \begin{bmatrix} \omega_1 & \omega_2 \\ \omega_2 & \omega_3 \end{bmatrix} = \begin{bmatrix} .01 & 0 \\ 0 & .01 \end{bmatrix} \\
&\boldsymbol{\alpha}_i = \begin{bmatrix} \alpha_1 & \alpha_2 \\ \alpha_2 & \alpha_3 \end{bmatrix} = \begin{bmatrix} .1 & .1 \\ .1 & .1 \end{bmatrix} + \begin{bmatrix} U(0-x_i) & U(0-x_i) \\ U(0-x_i) & U(0-x_i) \end{bmatrix} \\
&\boldsymbol{\beta}_i = \begin{bmatrix} \beta_1 & \beta_2 \\ \beta_2 & \beta_3 \end{bmatrix} = \begin{bmatrix} .9 & .9 \\ .9 & .9 \end{bmatrix} - \boldsymbol{\alpha} + \begin{bmatrix} U(0-x_i) & U(0-x_i) \\ U(0-x_i) & U(0-x_i) \end{bmatrix} \\
&with\ x_1 = 0.01 \quad x_2 = 0.03 \quad x_3 = 0.06
\end{aligned}
$$

We generated these models 1000 times. At each repetition, the matrices $\boldsymbol{\alpha}_i$ and $\boldsymbol{\beta}_i$ are randomly generated summing up a constant matrix and a random matrix whose elements have a random uniform distribution ranging from 0 until 0.01, 0.03 and 0.06 for MODEL(1), MODEL(2) and MODEL(3), respectively. This has been done in order to measure the impact of the departure from the possible root cancellation case on the small sample properties of the SP estimator. It is relevant to note that, when generating $\boldsymbol{\alpha}_i$ and $\boldsymbol{\beta}_i$, we allow only positive definite matrices since this condition guarantee that H_t is positive definite. We considered one sample size of 1000 observations. The simulation employed three alternative estimators: The multivariate (i.e. bivariate) GARCH ML estimator, the ML-DCC (Engle, 2002) estimator and the SP-DCC estimator.

Results for the RMSE of the conditional correlation are reported in the box-plots as in Figure 4. Not surprisingly, the bivariate maximum likelihood has the best performance. The DCC routine reports also very good performance comparable with the bivariate likelihood; the SP estimator performance is also comparable with the other methods, depending on the parameterization choice. This is notwithstanding the SP-DCC model is an approximation for this specific framework. It is interesting to observe the change of performance across the different models. In particular, the SP estimator tends to suffer when the gap between the $\alpha_i + \beta_i$ gets wider as in MODEL(3). On the other hand, for MODEL(1) the performance of SP-DCC and DCC are very close, for MODEL(2) are similar, while some deterioration of SP performance can be noted for MODEL(3). As the case of root cancellation is rather frequent in empirical applications, we expect MODEL(1) and MODEL(2) being indicative of the empirical performance of SP-DCC with real data. Here, indeed, the sums $\alpha_i + \beta_i$ might even tend to approach one.

The Integrated GARCH process arises when $(\alpha_i + \beta_i) = 1$. For this case, the SP-DCC model is no more an approximation. Indeed, for this case, any combination of model (35) preserve the ARMA(1,1) parametrization and therefore any combination of y_{1t} and y_{2t} also preserve the IGARCH(1,1) structure. As a consequence the SP estimator use the correct specification to estimate the conditional correlations. These considerations have been tested through some Monte Carlo simulations.

We generated model (31)-(32) assuming that the conditional covariance matrix follows an Integrated GARCH dynamics (IGARCH(1,1)). We considered a single decay factor driving the dynamics of the conditional covariance such that the following three parameters structures are considered:

$$
\begin{array}{l}
MODEL(j)\ for\ j = 4,5,6 \\
\boldsymbol{\omega}_j = 0.0001 * \left[\begin{array}{cc} 1 & 1 \\ 1 & 1 \end{array} \right] + \left[\begin{array}{cc} U(0-x_j) & 0 \\ 0 & U(0-x_j) \end{array} \right] \\
\boldsymbol{\alpha}_j = \left[\begin{array}{cc} 0.05 & 0.05 \\ 0.05 & 0.05 \end{array} \right] + \left[\begin{array}{cc} U(0-x_j) & U(0-x_j) \\ U(0-x_j) & U(0-x_j) \end{array} \right],\ \boldsymbol{\beta}_j = \left[\begin{array}{cc} 1 & 1 \\ 1 & 1 \end{array} \right] - \boldsymbol{\alpha}_j \\
with\ x_4 = 0.01\ \ x_5 = 0.03\ \ x_6 = 0.06
\end{array}
$$

The exercise compares the performance of four different competitors: 1) the pseudo-ML estimator as discussed in Zaffaroni (2008) that estimates a single decay factor (in the figures we define it as MLC), 2) the ML estimator that does not impose a single decay factor (in the figures we define it as ML), 3) the SP estimator, 4) the ML-DCC routine.

The reason for the inclusion of the ML estimator is that both SP and DCC do not impose the single decay factor. Therefore the interest in comparing three estimators that do not know the data generation process. The empirical results are reported in Figure 4. Since the performance of the models is unaffected by the selected parameterization, for reason of space we omit to report the results for the intermediate case (0.03). Beside the likelihood estimator (MLC) reporting the best results, for this case the SP estimator always performs better than DCC and even ML. This confirms that when the IGARCH(1,1) framework arises, SP represents a fully valid candidate in estimating the conditional correlations.

Now consider model (31)-(32) with the following unrestricted VECH representation:

$$
\left[\begin{array}{c} h_{1t} \\ h_{12t} \\ h_{2t} \end{array} \right] = \left[\begin{array}{c} \omega_1 \\ \omega_2 \\ \omega_3 \end{array} \right] + \left[\begin{array}{ccc} \beta_1 & \beta_2 & \beta_3 \\ \beta_4 & \beta_5 & \beta_6 \\ \beta_7 & \beta_8 & \beta_9 \end{array} \right] \left[\begin{array}{c} h_{1t-1} \\ h_{12t-1} \\ h_{2t-1} \end{array} \right] + \left[\begin{array}{ccc} \alpha_1 & \alpha_2 & \alpha_3 \\ \alpha_4 & \alpha_5 & \alpha_6 \\ \alpha_7 & \alpha_8 & \alpha_9 \end{array} \right] \left[\begin{array}{c} y_{1t}^2 \\ y_{1t}y_{2t} \\ y_{2t}^2 \end{array} \right] \tag{36}
$$

In this case neither the marginal processes y_{1t}^2, y_{2t}^2, $y_{1t}y_{2t}$, nor a combinations of them follows a ARMA(1,1) process. In addition, also the GARCH specifications of y_{1t} and y_{2t} do not follow a GARCH(1,1) model. For comparison purposes we generate the bivariate process as shown in Hafner (2008) p.476, in order to assess the performance of different competitors as above. Results comparing the RMSE of the conditional correlations are shown in Figure 4. Note that the model in (36) has 21 parameters and this represents a challenge for ML estimation. Indeed, given the problem of convergence faced by the numerical optimization, due to the high number of parameters, we decide to employ the true values of $\boldsymbol{\alpha}$ and $\boldsymbol{\beta}$ as initial values for the likelihood. This yields the MLC estimator and explains why the boxplot of the latter is far below the others. The ML estimator is the bivariate maximum likelihood estimator of a Diagonal VECH (as used before). The ML estimator is clearly an approximate likelihood as it estimate only the diagonal elements of model (36). Interestingly, the SP estimator seems to slightly outperform both the ML and the DCC routine in this latter case. This is a very interesting and promising result, given that this framework represents the most unrestricted case.

To conclude, the above promising results suggest that the SP-DCC model represents a simple and valid candidate regardless of the fact that it is an approximate model in general. Relative to competing approaches, such as the Engle (2002) DCC model, SP-DCC has the advantage that can be implemented regardless of the cross-sectional sample size, i.e. also for the case of vast set of conditionally heteroskedastic time series.

4 Estimation results

As described in the methodological section, the estimation of the SP-DCC model is performed using conditional mean residuals. In light of the model selection analysis, the latter are computed from the selected Adaptive-X-AR-IGARCH(1,1) models for the actual y_t series, yielding $\hat{\boldsymbol{\varepsilon}}_t = \left[\begin{array}{ccccccc} \hat{\varepsilon}_{GL,t} & \hat{\varepsilon}_{NH,t} & \hat{\varepsilon}_{SH,t} & \hat{\varepsilon}_{Trpcs,t} & \dots & \hat{\varepsilon}_{SOI,t} \end{array} \right]'$. IGARCH(1,1) models for the aggregates $y^+_{ij,t}$ and $y^-_{ij,t}$ are then estimated using the aggregated residuals $\hat{\varepsilon}^+_{ij,t}$ and $\hat{\varepsilon}^-_{ij,t}$.

Estimation of the decay factor for exponential smoothing in conditional variance is performed by means of cross-validation for computational easiness, yielding a persistence parameter estimate of 0.99 (not reported) for all cases. The results show that all the models are well specified and yield standardized residuals consistent with white noise properties. For reasons of space, we do not report details for the 81 IGARCH(1,1) models estimated for the actual and aggregate variables. A summary of the results is provided in Figure 5, where Boxplots for the p-value of the Box-Ljung tests for serial correlation and conditional heteroskedasticity, carried out using the standardized residuals, are plotted. Consistent with the diagnostics reported in Table 3 for the original y_t series, the IGARCH(1,1) model properly accounts for conditional heteroskedasticity also in the aggregate temperature anomaly series $y^+_{ij,t}$ and $y^-_{ij,t}$, as standardized residuals behaves according to white noise processes.

Very accurate is also the estimation of the conditional correlation processes as the third step correction is not required for the current application; given the single decay factor the IGARCH (1,1) specification of the conditional variance covariance matrix, positive definiteness at each point in time should indeed be expected, also consistent with the standard Riskmetrics-Exponential smoothing parameterization. Comparison with the Constant Conditional Correlation model of Bollerslev (1990), does support the modeling of time-varying conditional correlations. The SP-DCC model is in fact preferred to the CCC model, yielding a lower BIC information criterion, i.e. -9.5651 versus -9.2682 (not reported). Similarly SP-DCC is preferred to Engle (2002) DCC model, yielding a BIC equal to -9.3973 (not reported).[15] The latter findings provide support to the modeling of time-varying rather than constant conditional correlations across temeperature series. Moreover, it is fully consistent with the findings of the Monte Carlo analysis, showing the SP-DCC model to outperform Engle (2002) DCC model in a similar parametric framework.

4.1 Contemporaneous conditional correlations

In Figures 6-8 we plot the estimated (contemporaneous) conditional correlations across temperature anomaly series. For comparison we also include the Oceanic Niño Index (ONI). The latter is the standard that the National Oceanic and Atmospheric Administration - US Deparment of Commerce (NOAA) uses for identifying El Niño (warm) and La Niña (cool) events in the tropical Pacific.[16] Hence, an El Niño event refers to the warm

[15] Details are available upon request from the authors.

[16] The ONI is computed as the running 3-month mean SST anomaly for the Niño 3.4 region (i.e., 5^oN-5^oS, 120^o-170^oW). Events are defined as 5 consecutive overlapping 3-month periods at or above the $+0.5^o$ anomaly for warm (El Niño) events and at or below the -0.5 anomaly for cold (La Niña) events. The threshold is further broken down into Weak (with a 0.5 to 0.9 SST anomaly), Moderate (1.0 to 1.4), Strong (1.5 to 1.9) and Very Strong ($\geq$ 2.0) events. Data are available at http://www.cpc.noaa.gov/products/analysis_monitoring/ensostuff/ensoyears.shtml.

and negative phase of the El Niño and Southern Oscillation (ENSO), while a La Niña event refers to its cool and positive phase. The two components of ENSO, i.e. sea surface temperature and atmospheric pressure, are strongly related. During an El Niño event, the easterly trade winds converging across the equatorial Pacific weaken. This in turn slows the ocean current that draws surface water away from the western coast of South America and reduces the upwelling of cold water from the deeper ocean, allowing warm surface water to build in the eastern part of the basin. The strengthening and weakening of the trade winds is determined by changes in the pressure gradient of the atmosphere over the tropical Pacific. Yet, the warming of the sea surface triggers a decrease in the atmospheric pressure above it by transferring more heat to the atmosphere and increasing its intensity. Hence, the pressure gradient affects the sea surface temperatures and the sea surface temperatures affect the pressure gradient.

ENSO can affect zones thousands of kilometers away from the equatorial Pacific through the "atmospheric bridge". During El Niño events, heat transfer to the troposphere is magnified over the anomalously warm sea surface temperature; this in turn generates Rossby waves that propagate poleward and eastward and are subsequently refracted back from the pole to the tropics. The planetary waves form at preferred locations both in the North and South Pacific Ocean, and the teleconnection pattern is established within 2-6 weeks. Given that the teleconnection is mostly occurring within-month, we expect the (contemporaneous) conditional correlation analysis to be informative about the response of temperature anomalies to ENSO shocks.

In Figure 6 we then plot the conditional correlation of the SOI index versus temperature anomalies of various zones, while in Figures 7-8 we plot the conditional correlations across anomalies for various zones. In order to relate correlation dynamics to the magnitude of El Niño and La Niña events, in the plot we also include the ONI.

As shown in Figure 6, interesting patterns are revealed by the correlation analysis, overall consistent with ENSO effects in the Tropics and its teleconnection. Firstly, the conditional correlation versus the Tropics is largest, up to -0.2 and mostly negative in sign, consistent with El Niño (La Niña) events, i.e. a sizably negative (positive) SOI, leading to a warm (cool) phase in the Tropics. Coherent with the working of the "atmospheric bridge", a negative correlation can also be noted versus the Northern Polar, up to -0.2, over almost the whole sample. In both cases, the very strong El Niño events of 2014-2016 and 1997-1998 have made the conditional correlation more negative, i.e they have henanced the heat transfer. This is consistent with the general recognition that ENSO is an asymmetric phenomenon and that extreme ENSO events are different from moderate events (Cai et al., 2015a,b; 2014; Kim et al., 2014). Secondly, the conditional correlation of SOI versus NoExt is positive (0.1) and sizably increases since the mid-2000s (0.2), while the conditional correlations of SOI versus SoPol becomes persistently negative since mid/end-2000s. Thirdly, while the correlation of SOI versus SoExt has been on average positive over the sample investigated, it has steadily decreased over time, becoming even negative in the mid-2000s. Due to aggregation, not surprisingly the conditional correlation of SOI versus GL and NH (SH) show similar propertied than for NoExt (Trpcs and SoExt).

As shown in Figure 7, over the assessed sample conditional correlations of GL versus various zones are always positive, albeit the magnitude range is sizable (0.2-0.8). Surely interesting is the upward trend in the correlation between SoPol and GL, and between NH and SH, pointing to an increasing comovement over time of temperature anomalies for the latter zones; similarly interesting is the downward trend in the correlation between

NoPol and GL.

Moreover, as shown in Figure 8, a consistent pattern with ENSO teleconnections is also shown by the coditional correlations relating the various anomalies across zones. Conditional correlations are in fact positive over the whole sample for Trpcs versus NoExt and SoExt (0.10), and for NoExt versus NoPol, SoExt versus SoPol (0.3 to 0.5). The latter pattern is consistent with a warming shock being transmitted from the Tropics to the other zones, i.e. to the Extratropics and then to the Poles. A direct connection between the Tropics and the Poles is also detected; the latter correlations are however rather unstable and weak at the end of sample, apart from the sizable increase observed during the 2014-2016 very strong El Niño event.

Overall, while the general pattern revealed by the conditional correlation analysis is consistent with ENSO and ENSO-like long lived episodes, such as the Pacific Decadal Oscillation (PDO), which generate in the Tropics and then propagate to the Extratropics and the Poles through various teleconnection mechanisms, the analysis also point to some changes in the linkages relating anomalies across zones and the global propagation of ENSO events. Some of these changes appear to have been ongoing since at least the 1980s, i.e. the beginning of sample; others have occurred since the early/mid-2000s. Whether the observed changes can be related to global warming is surely an issue that deserves a careful assessment. In this respect, it is worth noting that, while no consensus view has emerged to date, changes in the amplitude and frequency of ENSO events and shifts in their teleconnections should indeed be expected, both as consequences of mean climate state changes (Cai et al., 2015a,b; 2014; and Kim et al., 2014; Ng et al., 2015; Coumou and Rahmstorf, 2012).

5 Conclusions

Much attention has recently been paid to potential changes in temperature anomalies, particularly with reference to an upward drift detectable for the entire globe and various zones since the mid-/late 1990s and to its possible connection to very strong concurrent El Niño/ENSO events. The latter drift would appear to have even further increased as a consequence of the most recent 2015-2016 very strong El Niño event. Despite El Niño events affect the global climate and disrupts normal weather patterns, it is however in general agreed that ENSO might contribute little of the global mean warming trend since the 1950s (Foster et al., 2009). The latter warming trend is in general related to radiative forcing, both of natural and anthropogenic origin, whose stochastic or deterministic nature has been contended in the literature since the early 1990s. More recently the debate has also focused on the implications of global warming for the frequency and amplitude of natural variability oscillations, such as ENSO and IOD. While no consensus view has emerged to date, it is however expected that their amplitude, frequency and teleconnections might change as consequences of global warming (Cai et al., 2015a,b; 2014; and Kim et al., 2014; Ng et al., 2015; Coumou and Rahmstorf, 2012).

In light of the above issues in this paper we further assess the linkages between temperature anomalies, radiative forcing and ENSO. The paper innovates the available literature in various directions. We find that temperature anomalies since the 1980s are best described by a short memory process about a single level shift occurring in the mid-/late 1990s. While the latter could in principle be related to concurrent very strong El Niño events, we however find stronger evidence for its connection to radiative forcing. By

means of a new flexible trend modeling approach, we uncover a nonlinear linkage between radiative forcing and temperature anomalies. The nonlinear trend closely tracks the low frequency evolution in temperature anomalies, also accounting for the mid-end 1990s level switch, the 1998-2013 "warming hiatus" and the current steepening in trend temperatures. Moreover, we find that radiative forcing also accounts for trend dynamics in SOI, therefore providing evidence that global warming might affect natural variability oscillations such as ENSO, and therefore contribute to their disruptive effects.

In the paper we also document the feature of time-varying volatility of temperature anomalies. The feature is well described by an IGARCH process, pointing to volatility clusters in temperature anomalies. The same feature is uncovered for SOI. In this respect, a sizable increase in SOI volatility can be noted since mid-2000s, concurrent with a somewhat earlier decrease in volatility for temperature anomalies and the steepening in the radiative forcing trend, consistent with feedback effects of global warming on natural variability oscillations.

The detected GARCH properties for temperature anomalies and SOI are then further assessed in the framework of a new dynamic conditional correlation model, i.e. the Semiparametric-DCC model (SP-DCC; Morana, 2015), which allows for the modeling of time-varying linkages across temperature series and in relation to ENSO. The proposed SP-DCC model is shown to compare favorably to exact ML and Engle (2002) DCC model in a Monte Carlo analysis.

We then document the presence of time-varying conditional correlations relating temperature anomalies across various zones and SOI. In this respect we find a correlation pattern consistent with ENSO effects in the Tropics and its teleconnections. Despite the latter findings, the analysis also reveals some important changes in the conditional correlation patterns involving SOI and temperature anomalies across zones. Some of these changes appear to have been ongoing since at least the 1980s, i.e. the beginning of sample; others have occurred since the early/mid-2000s. Whether the observed changes can be related to likely effects of global warming on the amplitude and frequency of ENSO events and on their teleconnections is surely an issue that deserves a careful assessment, which is however outside the scope of this paper.

References

[1] Angell, J.K., 1981. Comparison of variations in atmospheric quantities with sea surface temperature variations in the equatorial eastern Pacific. Monthly Wheather Review 109, 230-243.

[2] Baillie, R.T., Chung, S-K., 2002. Modeling and forecasting from trend-stationary long memory models with applicationd to climatology. International Journal of Forecastig 18, 215-226.

[3] Baillie, R.T., Morana, C., 2009. Modeling long memory and structural breaks in conditional variances: An Adaptive FIGARCH approach. Journal of Economic Dynamics and Control 33, 1577-1592.

[4] Baillie, R.T., Morana, C., 2002. Adaptive ARFIMA models with applications to inflation, Economic Modelling 29, 2451-2459.

[5] Becker, R., Enders, W., Lee, J., 2006. A stationarity test in the presence of an unknown number of smooth breaks. Journal of Time Series Analysis 27, 381-409.

[6] Bloomfield, P., 1992. Trends in global temperature. Climatic Change 21, 1-16.

[7] Bollerslev, T., 1986. Generalized autoregressive conditional heteroskedasticity. Journal of Econometrics 31, 302-327.

[8] Bollerslev, T., 1990. Modeling the coherence in short-run nominal exchange rates: A multivariate generalized ARCH model. Review of Economics and Statistics 72, 498-505.

[9] Bollerslev, T., Engle, R. and Wooldridge, J., 1998. A capital asset pricing model with time varying covariances. Journal of Political Economy 96, 116-131.

[10] Cai, W., Borlace S., Langaigne, M., van Rensch, P., Collins, M., Vecchi, G., Timmermann, A., Santoso, A., McPhaden, M.J., Wu., L., England, M.H., Wang, G., Guilyardi, E., Jin, F.-F., 2014. Increased frequency of extreme El Niño events due to greenhouse warming. Nature Climate Change 4, 1-6.

[11] Cai, W., Santoso A., Wang, G., Yeh, S.-W., An, S.-I., Cobb, K., Collins, M., Guuilyardi, E., Jin, F.-F., Kung, J.-S., Lengaigne, M., McPhaden, M.J., Takahashi, K., Timmermann, A., Vecchi, G., Watanabe, M., Wu., L., 2015a. ENSO and greenhouse warming. Nature Climate Change 5, 849-859.

[12] Cai, W., Wang, G., Santoso, A., McPhaden, M., Wu, L., Jin, F.-F., Timmermann, A., Collins, M., Vecchi., G., Langaigne, M., England, M.H., Dommenget, D., Takahashi, K., Guilyardi, E., 2015b. Increased frequency of extreme La Nina events under greenhouse warming. Nature Climate Change 5, 132-137.

[13] Chang, Y., Kaufmann, R.K., Kim, C.S., Miller, J.I., Park, J.Y., Park, S., 2016. Time series analysis of global temperature distributions: Identifying and estimating persistent features in temperature anomalies. Boston University, mimeo.

[14] Christy, J.R., McNider, R.T., 1994. Satellite greenhouse signal. Nature 367, 325.

[15] Christy, J.R., Spencer, R.W., Norris, W.B., 2011. The role of remote sensing in monitoring global bulk tropospheric temperatures. International Journal of Remote Sensing 32, 671-685.

[16] Cohen, J., Barlow, M., 2005. The NAO, AO and global warming: How closely related. Journal of Climate 18, 4498-4513.

[17] Coumou, D., Rahmstorf, S., 2012. A decade of weather extremes. Nature Climate Change 2, 1-6.

[18] Diebold, F.X., Inoue, A., 2001. Long memory and regime switching. Journal of Econometrics 105, 131-159.

[19] Douglass, D.H., Christy, J.R., 2009. Limits on CO_2 climate forcing from recent temperature data on earth. Energy and Environment 20, 177-189.

[20] Enders, W., Lee, J., 2012. A unit root test using a Fourier series to approximate smooth breaks. Oxford Bulletin of Economics and Statistics 74. 574-599.

[21] Engle, R.F., 2002. Dynamic Conditional Correlation - A simple class of multivariate GARCH models. Journal of Business and Economic Statistics, 20, 339-350.

[22] Estrada, F., Perron, P., 2016. Extracting and analyzing the warming trend in global and hemispheric temperatures. Boston University, mimeo.

[23] Foster, G., Annan, J.D., Jones, P.D., Mann, M.E., Mullan, B., Renwick, J., Salinger, J., Schmidt, G.A., Trenberth, K.E., 2010. Comment on "Influence of the Southern Oscillation on tropospheric temperature". Journal of Geophysical Research 115, 1-4.

[24] Gallant, A.R., 1981. On the bias in flexible functional forms and an essentially unbiased form: the Fourier flexible form. Journal of Econometrics 15, 211-245.

[25] Gay, C., Estrada, F., Sánchez, A., 2009. Global and hemispheric temperatures revisited. Climatic Change 94, 333-349.

[26] Granger, C.W.J., 1980. Long memory relationships and the aggregation of dynamic models. Journal of Econometrics 14, 227-238.

[27] Hafner, C.M., 2008. Temporal aggregation of multivariate GARCH models. Journal of Econometrics

[28] 142, 467-483.

[29] Harvey, D.I., Mills, T.C., 2001. Modeling global temperature using cointegration and smooth transitions. Statistical Modeling 1, 143-159.

[30] Jones, P.D., 1989. The influence of ENSO on global temperature. Climate Monitoring 17, 80-89.

[31] Kaufmann, R.K., Stern, D.I., 1997. Evidence for human influence on climate from hemispheric temperature relations. Nature 388, 39-44.

[32] Kaufmann, R.K., Stern, D.I., 2002. Cointegration analysis of hemisphere temperature relations. Journal of Geophysical Research 107, 1-10.

[33] Kaufmann R.K., Kauppi, H., Stock, J.H., 2006. The relationship between radiative forcing and temperature: what do statistical analyses of instrumental temperature record measure? Climate Change 77, 279-289.

[34] Kaufmann R.K., Kauppi, H., Mann, M.L., Stock, J.H., 2013. Does temperature contains a stochastic trend: linking statistical results to physical mechanisms. Climatic Change 118, 729-743.

[35] Kim, S.T., Cai, W., Jin, F.-F., Santoso, A., Wu, L., Guilyardi, E., An, S.I., 2014. Response of El Niño sea surface temperatures to greenhouse warming. Nature Climate Change 4, 786-790.

[36] Kosaka, Y., Xie, S.P., 2013. Recent global-warming hiatus tied to equatorial Pacific surface cooling. Nature 501, 403-407.

[37] Ledoit, O., Wolf, M., 2012. Nonlinear shrinkage estimation of large-dimensional covariance matrices. The Annals of Statistics 40, 1024-1060.

[38] Liu H., Rodríguez G., 2005. Human activities and global warming: a cointegration analysis. Environmental Modelling Software 20, 761-773.

[39] Mann, M.E., 2011. On long range dependence in global surface temperature series. An editorial comment. Climatic Change 107: 267-276.

[40] Mayadunne G., Evans M., Inder B., 1995. An empirical investigation of shock persistence in economic time series. Economic Records 71, 145-156.

[41] McKitrick, R.R., Vogelsang, T.J., 2014. HAC robust trend comparisons among climate series with possible level shifts. Environmetrics 25, 528-547.

[42] McLean, J.D., de Freitas, C.R., Carter, R.M., 2009. Influence of the Southern Oscillation on tropospheric temperature. Journal of Geophysical Research 114, 1-8.

[43] Mills T.C., 2006. Modelling current trends in Northern Hemisphere temperatures. International Journal of Climatology 26, 867-884.

[44] Mills T.C., 2013. Breaks and unit roots in global and hemispheric temperatures: Aan updated analysis. Climatic Change 118, 745-755.

[45] Morana, C., 2015. Semiparametric Estimation of Multivariate GARCH Models, Open Journal of Statistics 5, 852-858.

[46] Mosedale TJ, Stephenson DB, Collins M, Mills TC (2006) Granger causality of coupled climate processes: ocean feedback on the North Atlantic oscillation. J Clim 19:1182–1194.

[47] Ng, B., Cai, W. Walsh, K., Santoso, A., 2015. Nonlinear processes reinforce extreme IOD events. Scientific Reports 5, 1-10.

[48] Parke, W.R., 1999. What is fractional integration? The Review of Economics and Statistics 81,632-638.

[49] Pelletier J.D., Turcotte, D.L., 1997. Long-range persistence in climatological and hydrological time series: analysis, modeling and application to drought hazard assessment. Journal of Hydrology 203, 198-208.

[50] Perron, P., Shintani, M, Yabu, T., 2016. Testing for flexible nonlinear trends with an integrated or stationary noise component. Oxford Bulletin of Economics and Statistics, forthcoming.

[51] Pretis, F., Mann, M.L., Kauffman, R.K., 2015. Testing competing models of the temperature hiatus: assessing the effects of conditioning variables and temporal uncertainties through sample-wide break detection. Climatic Change 131, 705-718.

[52] Rea, W., Reale, M., Brown, J., 2011. Long memory in temperature reconstructions. Climatic Change 107, 247-265.

[53] Schmith, T., Johansen, S., Thejll, P., 2012. Statistical analysis of global surface temperature and sea level using cointegration methods. Journal of Climate 25, 7822-7833.

[54] Stern DI, Kaufmann RK (1999) Econometric analysis of global climate change. Environ Modell Softw 14:597–605

[55] Stern D.I., Kaufmann, R.K., 2000. Detecting a global warming signal in hemispheric series: A structural time series analysis. Climatic Change 47, 411-438.

[56] United Nations Office for the Coordination of Humanitarian Affairs, 2016. El Niño CERF-funded response in 2015-2016, 1 April 2016.

[57] Wigley, T.M.L., 2000. ENSO, volcanoes, amd record breaking temperatures, Geophysical Research Letters 27. 4101-4104.

[58] Wilks DS (2011) Statistical methods in the atmospheric sciences. Academic, New York

[59] WMO (1966) Climatic change. WMO technical note 79. World Meteorological Organization, Geneva

[60] Zaffaroni, P., 2008. Large scale volatility models: Theoretical properties of professionals' practice. Journal of Time Series Analysis 29, 581-599.

[61] Zheng, X., Basher, R.E., 1999. Structural time series models and trend detection in global and regional temperature series. Journal of Climate 12, 2347-2358.

Table 1: Persistence analysis of temperature anomaly series

Panel A: ADF tests									
		GL	**NH**	**SH**	**Trpcs**	**NoExt**	**SoExt**	**NoPol**	**SoPol**	**SOI**
Constant+Trend		-5.737	-6.684	-7.200	-5.910	-8.141	-7.104	-9.243	-15.01	-5.877
Constant		-4.493	-4.607	-4.738	-5.174	-4.637	-5.876	-6.126	-15.03	-5.780
No costant		-4.418	-4.543	-4.684	-5.104	-4.583	-5.811	-6.024	-14.86	-5.699
Panel B: Structural break analysis										
		GL	**NH**	**SH**	**Trpcs**	**NoExt**	**SoExt**	**NoPol**	**SoPol**	**SOI**
UD-max		44.120	92.867	33.397	64.821	103.22	34.724	41.711	33.939	42.709
LWZ – 0		-2.971	-2.354	-3.078	-2.614	-2.106	-2.698	-3.025	-1.925	-3.137
LWZ – 1		-3.363	**-2.759**	-3.373	-3.018	**-2.463**	-2.981	**-3.264**	**-2.057**	-3.352
LWZ – 2		-3.405	-2.741	**-3.434**	**-3.072**	-2.446	**-3.062**	-3.252	-2.018	**-3.358**
LWZ – 3		**-3.407**	-2.722	-3.427	-3.062	-2.417	-3.049	-3.228	-1.988	-3.347
LWZ – 4		-3.402	-2.726	**-3.438**	-3.041	-2.397	-3.038	-3.213	-1.956	-3.343
LWZ – 5		-3.385	-2.705	-3.422	-3.039	-2.382	-3.017	-3.198	-1.916	-3.316
SupF(2|1)		9.087	7.124	9.793	7.677	8.724	11.431	10.227	3.023	12.855
Break dates		**1997:6**	**1997:8**	**1995:3**	**1997:6**	**1998:1**	**1997:6**	**1995:3**	**1995:3**	**1995:3**
Panel C: Long memory models: estimated fractional differencing parameter and AIC, BIC										
		GL	**NH**	**SH**	**Trpcs**	**NoExt**	**SoExt**	**NoPol**	**SoPol**	**SOI**
Mod 1	***d***	0.665 (0.039)	0.580 (0.039)	0.566 (0.044)	0.877 (0.048)	0.478 (0.035)	0.373 (0.038)	0.277 (0.033)	0.259 (0.053))	0.536 (0.043)
	AIC	-1.4522	-0.8548	-1.0279	**-0.9257**	-0.3339	-0.5602	1.5666	**1.8251**	**2.1598**
	BIC	**-1.4521**	**-0.8278**	**-1.0008**	**-0.8987**	-0.3068	-0.5331	1.5937	**1.8525**	**2.1869**
Mod 2	***d***	0.646 (0.042)	0.545 (0.043)	0.544 (0.047)	0.865 (0.049)	0.418 (0.043)	0.3365 (0.044)	0.1958 (0.044)	0.260 (0.053)	0.533 (0.044)
	AIC	-1.4527	**-0.8624**	-1.0309	-0.9257	**-0.3528**	-0.5660	1.5412	1.8290	2.1603
	BIC	-1.4166	-0.8263	-0.9947	-0.8896	**-0.3167**	-0.5299	1.5773	1.8651	2.1964
Mod 3	***d***	0.645 (0.043)	0.551 (0.042)	0.5419 (0.046)	0.875 (0.049)	0.432 (0.042)	0.334 (0.043)	0.201 (0.044)	0.260 (0.053)	0.536 (0.044)
	AIC	**-1.4540**	-0.8598	**-1.0319**	-0.9218	-0.3459	**-0.5722**	**1.5401**	1.8292	2.1642
	BIC	-1.4179	-0.8237	-0.9958	-0.8857	-0.3098	**-0.5361**	**1.5762**	1.8653	2.2002
Mod 4	***d***	0.645 (0.043)	0.539 (0.042)	0.538 (0.046)	0.864 (0.049)	0.413 (0.043)	0.331 (0.044)	0.186 (0.045)	0.260 (0.053)	0.531 (0.044)
	AIC	-1.4522	-0.8615	-1.0302	-0.9216	-0.3516	-0.5683	1.5392	1.8334	2.1639
	BIC	-1.4070	-0.8164	-0.9851	-0.8764	-0.3064	-0.5232	1.5844	1.8785	2.2090
Panel D: Short memory models: estimated persistence parameter and AIC, BIC										
		GL	**NH**	**SH**	**Trpcs**	**NoExt**	**SoExt**	**NoPol**	**SoPol**	**SOI**
Mod 1	$\sum \phi_i$	0.887 (0.064)	0.850 (0.065)	0.801 (0.062)	0.867 (0.026)	0.790 (0.065)	0.611 (0.063)	0.513 (0.071)	0.331 (0.047)	0.790 (0.095)
	AIC	-1.4748	-0.8569	-1.0325	-0.9714	-0.3068	-0.5270	1.6295	**1.7901**	**2.1100**
	BIC	-1.4478	-0.8298	-1.0054	**-0.9533**	-0.2685	-0.4999	1.6566	**1.8081**	**2.1462**
Mod 2	$\sum \phi_i$	0.818 (0.064)	0.748 (0.065)	0.718 (0.063)	0.867 (0.025)	0.624 (0.066)	0.491 (0.065)	0.309 (0.071)	0.331 (0.047)	0.777 (0.093)
	AIC	**-1.4970**	-0.8876	**-1.0595**	**-0.9743**	**-0.3660**	**-0.5702**	1.5592	1.7987	2.1128
	BIC	**-1.4519**	**-0.8425**	**-1.0144**	-0.9382	**-0.3209**	**-0.5250**	**1.5973**	1.8348	2.1670
Mod 3	$\sum \phi_i$	0.818 (0.065)	0.753 (0.065)	0.724 (0.063)	0.867 (0.026)	0.641 (0.066)	0.497 (0.065)	0.318 (0.070)	0.332 (0.047)	0.783 (0.093)
	AIC	-1.4945	-0.8871	-1.0568	-0.9733	-0.3586	-0.5699	1.5502	1.7987	2.1164
	BIC	-1.4494	-0.8420	-1.0117	-0.9373	-0.3134	-0.5248	1.5953	1.8348	2.1705
Mod 4	$\sum \phi_i$	0.818 (0.065)	0.738 (0.065)	0.712 (0.063)	0.865 (0.025)	0.612 (0.066)	0.483 (0.065)	0.292 (0.071)	0.331 (0.047)	0.776 (0.094)
	AIC	-1.4974	**-0.8898**	-1.0587	-0.9716	-0.3682	-0.5709	**1.5453**	1.8030	2.1169
	BIC	-1.4433	-0.8357	-1.0046	-0.9264	-0.3141	-0.5168	1.5994	1.8481	2.1801

Panel A reports the ADF nonstationarity tests for three different specifications of the deterministic component, i.e. constant plus trend, only constant and no constant and trend. The 5% and 1% critical values are -3.42 and -3.98, -2.87 and -3.45, -1.94 and -2.57, respectively.

Panel B reports the results of the Bai-Perron (1998) UD-Max structural break test. The 5% and 1% critical values of the test are 9.63 and 13.58, respectively. It also reports the LZW information criterion for the case of *n* breaks, *n* = 0, …, 5 (LWZ-*n*) and the SupF test for the null of 1 break against the alternative of 2 breaks; the 5% and 1% critical values of the test are 11.14 and 15.03, respectively. The date of the selected break point is finally reported.

Panel C reports the estimated fractional differencing parameter and the AIC and BIC information criteria for four different ARFIMA(0,*d*,0) models, with constant mean (Model 1), with switching intercept according to the estimated break date by the Bai-Perron UD-max tests (Model 2), with linear time trend (Model 3), with switching intercept and linear trend (Model 4).

Panel D reports the estimated persistence parameter and the AIC and BIC information criteria for four different AR(p) models, with constant mean (Model 1), with switching intercept according to the estimated break date by the Bai-Perron UD-max tests (Model 2), with linear time trend (Model 3), with switching intercept and linear trend (Model 4).

The series investigated are average land and ocean temperature anomalies for the entire globe (GL; 90S-90N) and seven zones, namely the Northern Hemisphere (NH; 0-90N), the Southern Hemisphere (SH; 90S-0), the Tropics (Trpcs; 20S-20N), the Northern Extratropic (NoExt; 20N-90N), the Southern Extratropic (SoExt; 90S-20S), the Northern Polar (NoPol; 60N-90N), the Southern Polar (SoPol; 90S-60S).

Table 2: Nonlinearity Perron-Shintani-Yabu Wald test

Panel A: Nonlinearity Wald test									
Linear trend included									
	GL	**NH**	**SH**	**Trpcs**	**NoExt**	**SoExt**	**NoPol**	**SoPol**	**SOI**
Order 1	0.2115	0.1525	0.3875	0.2444	0.4703	0.3766	0.4538	0.2389	0.7533
Order 2	1.8328	2.3552	1.6595	0.6015	2.5347	1.6943	**3.6086**	0.2324	0.4455
Order 3	0.4455	0.6194	0.5068	0.1177	0.7229	2.2714	0.4095	2.4189	2.2155
Order 4	1.7901	3.1143	1.0085	0.7004	**5.7330**	1.9144	0.9017	1.2853	2.2660
Order 5	1.3772	0.8313	2.1692	0.6824	0.4355	**3.2445**	**3.3590**	**4.0325**	0.4617
Linear trend omitted									
	GL	**NH**	**SH**	**Trpcs**	**NoExt**	**SoExt**	**NoPol**	**SoPol**	**SOI**
Order 1	**5.3457**	**7.2277**	**5.0177**	1.7042	**6.3493**	**5.2017**	**24.3710**	0.1882	1.6183
Order 2	0.2764	0.3327	0.3878	0.4902	0.1205	0.2497	0.0068	0.2447	0.2792
Order 3	0.7138	0.6974	1.2227	0.3187	0.4115	2.5531	0.0196	2.6472	2.6040
Order 4	0.6002	0.7916	0.4654	1.6084	0.3701	0.2890	0.0253	1.3987	1.7171
Order 5	0.2821	0.0774	0.4747	0.3125	0.0290	0.5005	0.0871	**4.4988**	0.3049
Panel B: Adaptive-AR specifications									
	GL	**NH**	**SH**	**Trpcs**	**NoExt**	**SoExt**	**NoPol**	**SoPol**	**SOI**
$\sum \phi_i$	0.852 (0.065)	0.798 (0.066)	0.761 (0.063)	0.877 (0.025)	0.701 (0.066)	0.539 (0.064)	0.348 (0.073)	0.325 (0.047)	0.790 (0.095)
γ_1	-0.152 (0.052)	-0.187 (0.051)	-0.120 (0.039)	-0.130 (0.081)	-0.224 (0.045)	-0.109 (0.026)	-0.368 (0.050)	-	-
δ_3	-	-	-	-	-	-	-	0.089 (0.060)	-
AIC	-1.4850	-0.8742	-1.0447	-0.9723	-0.3394	-0.5539	1.5595	1.7893	2.1100
BIC	-1.4489	-0.8381	-1.0086	-0.9453	-0.3033	-0.5178	1.5956	1.8164	2.1462

Panel A reports the Perron-Shintani-Yabu nonlinearity Wald test for various orders of the Fourier expansion. The critical values are 3.2189, 4.6052, 5.9915, 9.2103 for the 20%, 10%, 5% and 1% critical value, respectively.

Panel B reports the estimated persistence parameter, the selected terms of the Fourier expansion and AIC and BIC information criteria for the Adaptive-AR models.

The series investigated are average land and ocean temperature anomalies for the entire globe (GL; 90S-90N) and seven zones, namely the Northern Hemisphere (NH; 0-90N), the Southern Hemisphere (SH; 90S-0), the Tropics (Trpcs; 20S-20N), the Northern Extratropic (NoExt; 20N-90N), the Southern Extratropic (SoExt; 90S-20S), the Northern Polar (NoPol; 60N-90N), the Southern Polar (SoPol; 90S-60S).

Table 3: Adaptive-X-AR-GARCH models

Panel A: AR-B - Bai-Perron break process specifications									
	GL	**NH**	**SH**	**Trpcs**	**NoExt**	**SoExt**	**NoPol**	**SoPol**	**SOI**
c_0	-0.095 (0.044)	-0.119 (0.044)	-0.104 (0.038)	-	-0.143 (0.037)	-0.075 (0.026)	0.247 (0.056)	-	-
c_1	0.244 (0.057)	0.302 (0.058)	0.218 (0.047)	0.145 (0.059)	0.367 (0.052)	0.182 (0.033)	0.541 (0.075)	-	-
ϕ_1	0.576 (0.047)	0.517 (0.049)	0.527 (0.045)	0.876 (0.023)	0.418 (0.049)	0.363 (0.044)	0.204 (0.057)	0.335 (0.047)	0.464 (0.055)
ϕ_2	0.244 (0.045)	0.234 (0.045)	0.193 (0.043)	-	0.206 (0.045)	0.131 (0.045)	0.098 (0.048)	-	0.205 (0.057)
ϕ_3	-	-	-	-	-	-	-	-	0.114 (0.053)
β	0.990 (0.0136)	0.990 (0.014)	0.990 (0.014)	0.990 (0.015)	0.990 (0.013)	0.990 (0.0189)	0.990 (0.018)	0.990 (0.022)	0.990 (0.023)
α	0.010 (-)	0.010 (-)	0.010 (-)	0.010 (-)	0.010 (-)	0.010 (-)	0.010 (-)	0.010 (-)	0.010 (-)
AIC homosk	-1.4970	-0.8876	-1.0595	-0.9757	-0.3660	-0.5702	1.5522	1.7944	2.1100
BIC homosk	-1.4519	-0.8425	-1.0144	-0.9486	-0.3209	-0.5250	1.5973	1.8215	2.1462
R2	0.749	0.677	0.590	0.793	0.578	0.334	0.251	0.110	0.502
AIC	-1.4932	-0.8798	-1.0565	-0.9728	-0.3599	-0.5704	1.5600	1.7911	2.1153
BIC	-1.4571	-0.8437	-1.0204	-0.9548	-0.3238	-0.5343	1.5961	1.8003	2.1514
$Q(20)$	0.9214	0.8257	0.5832	0.0209	0.7132	0.7115	0.1912	0.3565	0.2814
$Q(20)_2$	0.7577	0.2557	0.5857	0.4536	0.0812	0.7675	0.0761	0.5623	0.0006
BJ	0.0287	0.0000	0.7893	0.0664	0.0902	0.2865	0.0000	0.1198	0.0040
Joint Bias	0.9707	0.6057	0.9873	0.1007	0.9402	0.7981	0.1466	0.6440	0.2131
Joint Stability	0.3395	0.4858	0.4734	0.0972	0.5519	0.6194	0.8709	0.3163	0.6452
Panel B: Adaptive-X-AR models - Radiative forcing specifications									
	GL	**NH**	**SH**	**Trpcs**	**NoExt**	**SoExt**	**NoPol**	**SoPol**	**SOI**
c_0	-0.897 (0.205)	-1.059 (0.201)	-0.594 (0.170)	-0.632 (0.391)	-1.431 (0.142)	-0.758 (0.109)	-1.956 (0.244)	-	-
c_2	0.632 (0.135)	0.747 (0.133)	0.416 (0.109)	0.437 (0.255)	0.996 (0.094)	0.526 (0.070)	1.356 (0.163)	-	-
γ_3	-	-	-	-	0.121 (0.029)	0.046 (0.022)	0.217 (0.045)	-	-
γ_5 **or** γ_4 **(*)**	0.084 (0.034)	0.104 (0.039)		0.131 (0.074)	0.166 (0.032)	0.078 (0.035)	0.176 (0.055)	-	-0.436(*) (0.188)
δ_5 **or** δ_3 **(*)**	-	-	0.064 (0.028)	0.143(*) (0.075)	-	-	-	-	-
								-	
ϕ_1	0.574 (0.047)	0.512 (0.049)	0.521 (0.046)	0.862 (0.024)	0.370 (0.050)	0.331 (0.044)	0.206 (0.056)	0.335 (0.047)	0.455 (0.055)
ϕ_2	0.234 (0.046)	0.229 (0.046)	0.191 (0.043)	-	0.157 (0.049)	0.104 (0.046)	-	-	0.204 (0.057)
ϕ_3	-	-	-	-	-		-	-	0.116 (0.053)
β	0.990 (0.022)	0.990 (0.010)	0.990 (0.012)	0.990 (0.013)	0.990 (0.016)	0.990 (0.011)	0.990 (0.014)	0.990 (0.017)	0.990 (0.022)
α	0.010 (-)	0.010 (-)	0.010 (-)	0.010 (-)	0.010 (-)	0.010 (-)	0.010 (-)	0.010 (-)	0.010 (-)
AIC homosk	-1.5000	-0.8923	-1.0612	-0.9778	-0.4027	-0.5938	1.5414	1.7944	2.1031
BIC homosk	-1.4460	-0.8382	-1.0070	-0.9236	-0.3395	-0.5309	-1.5956	1.8215	2.1482
R2	0.751	0.680	0.593	0.796	0.596	0.355	0.263	0.110	0.508
AIC	-1.4967	-0.8843	-1.0596	-0.9742	-0.3958	-0.5935	1.5502	1.7911	2.1068
BIC	-1.4516	-0.8391	-1.0145	-0.9291	-0.3416	-0.5393	1.5953	1.8003	2.1429
$Q(20)$	0.9232	0.8964	0.6648	0.0265	0.8914	0.7290	0.2659	0.3565	0.3509
$Q(20)_2$	0.3807	0.0482	0.7132	0.5139	0.0292	0.8184	0.1987	0.5623	0.0008
BJ	0.0443	0.0000	0.9143	0.0110	0.0062	0.3246	0.0000	0.1198	0.0000
Joint Bias	0.8330	0.6376	0.9832	0.1217	0.6360	0.5083	0.0622	0.6440	0.1412
Joint Stability	0.3826	0.6615	0.8024	0.6670	1.1220	0.9001	1.8245	0.3163	0.6915

Table 3 (ctd.): Adaptive-X-AR-GARCH models

Panel C: Hybrid Adaptive-X-AR-B models									
	GL	**NH**	**SH**	**Trpcs**	**NoExt**	**SoExt**	**NoPol**	**SoPol**	**SOl**
c_0	-0.088 (0.041)	-0.111 (0.039)	-0.092 (0.020)	-0.083 (0.073)	-0.674 (0.191)	-0.495 (0.152)	-1.299 (0.361)	-	-
c_1	0.264 (0.055)	0.329 (0.055)	0.216 (0.039)	0.206 (0.096)	0.263 (0.064)	0.088 (0.048)	0.281 (0.113)	-	-
c_2	-	-	-	-	0.411 (0.144)	0.323 (0.113)	0.812 (0.275)	-	-
γ_3	-	-	-	-	-	-	0.156 (0.050)	-	-
γ_5 **or** γ_4 **(*)**	0.078 (0.032)	0.096 (0.036)	-	0.139(*) (0.036)	0.141 (0.032)	0.069 (0.024)	0.165 (0.053)	-	-0.436(*) (0.188)
δ_5 **or** δ_3 **(*)**	-	-	0.094 (0.025)	0.132(*) (0.076)	-	-	-	-	-
ϕ_1	0.564 (0.047)	0.500 (0.050)	0.497 (0.045)	0.859 (0.025)	0.368 (0.050)	0.334 (0.044)	0.184 (0.056)	0.335 (0.047)	0.455 (0.055)
ϕ_2	0.240 (0.045)	0.222 (0.046)	0.174 (0.044)	-	0.160 (0.047)	0.106 (0.047)	-	-	0.204 (0.057)
ϕ_3	-	-	-	-	-	-	-	-	0.116 (0.053)
β	0.990 (0.010)	0.990 (0.012)	0.990 (0.012)	0.990 (0.014)	0.990 (0.012)	0.990 (0.011)	0.990 (0.014)	0.990 (0.021)	0.990 (0.022)
α	0.010 (-)	0.010 (-)	0.010 (-)	0.010 (-)	0.010 (-)	0.010 (-)	0.010 (-)	0.010 (-)	0.010 (-)
AIC homosk	-1.5039	-0.8970	1.0798	-0.9804	-0.4023	-0.5913	1.5321	1.7901	2.1031
BIC homosk	-1.4549	-0.8429	-1.0257	-0.9263	-0.3391	-0.5281	1.5953	1.8081	2.1482
R2	0.752	0.682	0.600	0.796	0.595	0.359	0.273	0.110	0.498
AIC	-1.5000	-0.8889	-1.0787	-0.9771	-0.3956	-0.5907	1.5408	1.7911	2.1068
BIC	-1.4516	-0.8438	-1.0336	-0.9320	-0.3415	-0.5365	1.5949	1.8003	2.1429
$Q(20)$	0.9353	0.9135	0.6127	0.0275	0.8735	0.7869	0.3675	0.3565	0.3509
$Q(20)_2$	0.6489	0.2659	0.7329	0.5170	0.0707	0.8722	0.1407	0.5623	0.0008
BJ	0.0312	0.0000	0.9880	0.0321	0.0107	0.3185	0.0000	0.1198	0.0000
Joint Bias	0.8749	0.5416	0.9806	0.1417	0.3203	0.2965	0.3068	0.6440	0.1412
Joint Stability	0.5517	0.8002	0.6827	0.6554	0.8213	0.8967	1.8972	0.3163	0.6915

Panel A reports the ML estimated AR-B models including a step dummy variables with unitary values set according to the Bai-Perron UD-max structural break tests. Panel B reports the ML estimated Adaptive-X-AR models with radiative forcing control variables. Panel C reports the ML estimated hybrid Adaptive-X-AR-B models including both the Bai-Perron step dummy variable and radiative forcing control variables. R2 is the coefficient of determination. *AIC* (*homosk*) and *BIC* (*homosk*) are the Akaike and Bayes-Schwarz information criteria, respectively, computed for the conditionally heteroskedastic (homoscedastic) version of the models. $Q(20)$ and $Q(20)_2$ are the Box-Ljung test for serial correlation up to the 20*th* order in the standardized and squared standardized residuals, respectively. BJ is the Bera-Jarque normality test, Joint Bias is the Engle-Ng joint test for asymmetry in variance, Stability is the joint Nyblom stability test.

The series investigated are average land and ocean temperature anomalies for the entire globe (GL; 90S-90N) and seven zones, namely the Northern Hemisphere (NH; 0-90N), the Southern Hemisphere (SH; 90S-0), the Tropics (Trpcs; 20S-20N), the Northern Extratropic (NoExt; 20N-90N), the Southern Extratropic (SoExt; 90S-20S), the Northern Polar (NoPol; 60N-90N), the Southern Polar (SoPol; 90S-60S).

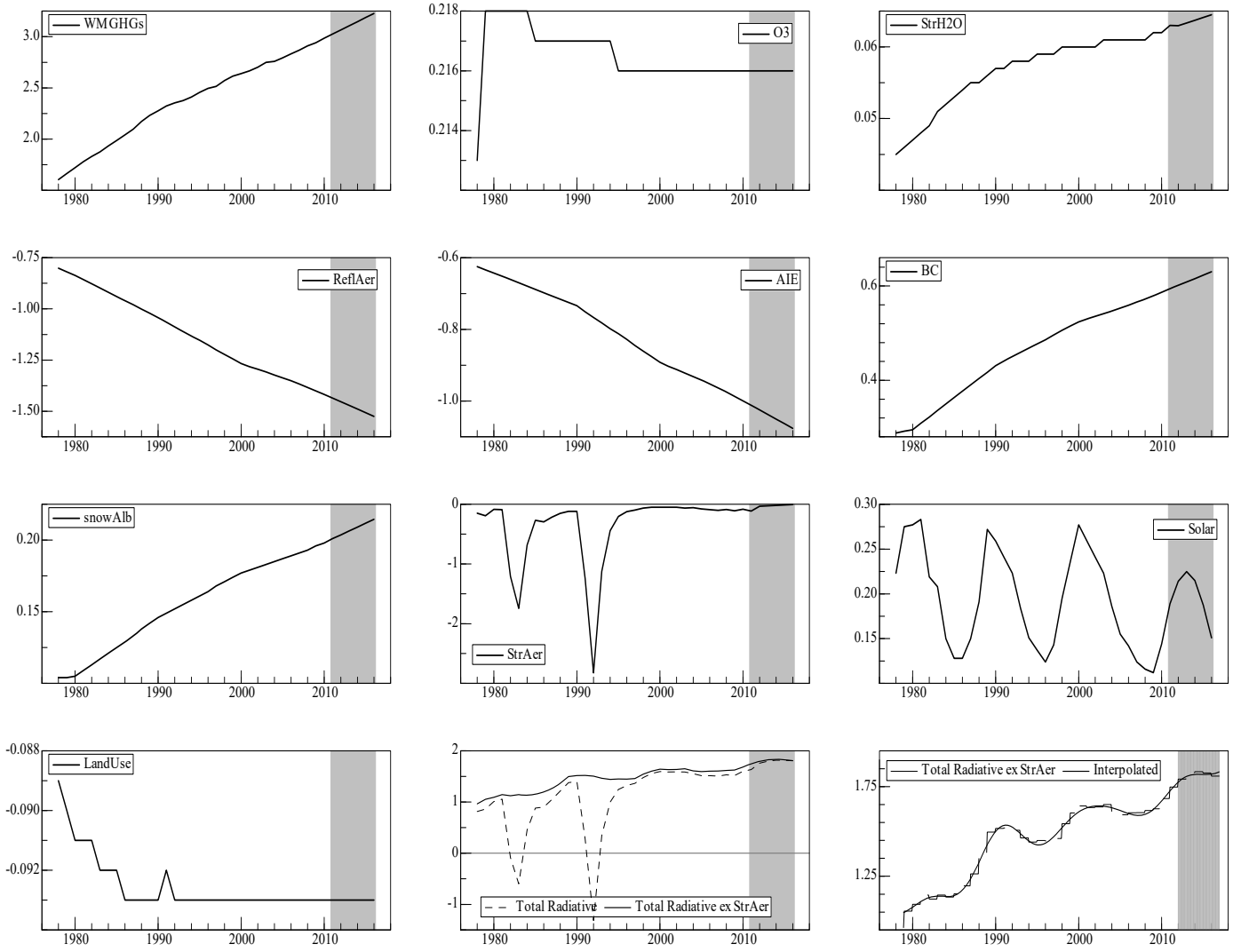

Figure 1: Radiative forcing components and total radiative forcing: actual data, forecasts for 2012-2016 (grey shadow), and monthly interpolated series (Interpolated). Following Hansen et al. (2005), radiative forcing has been decomposed in various categories, i.e., Well-Mixed Greenhouse Gases (WMGG; carbon dioxide (CO_2), methane (NH4), nitrous oxide (N2O) and chlorofluorocarbons (CFCs)), Ozone (O3), Stratospheric Water Vapor (StrH2O), Reflective Tropospheric Aerosols (ReflAer), Tropospheric Aerosol Indirect Effects (AIE), Black Carbon Aerosols (BC), Snow Albedo (snowAlb), Stratospheric Aerosols (StrAer), Solar Irradiance (Solar), Land Use (including irrigation; LandUse). In the plots, Total Radiative corresponds to the sum of the all the reported components; Total Radiative ex StrAer corresponds to the sum of all the reported components with Stratospheric Aerosols (StrAer) omitted.

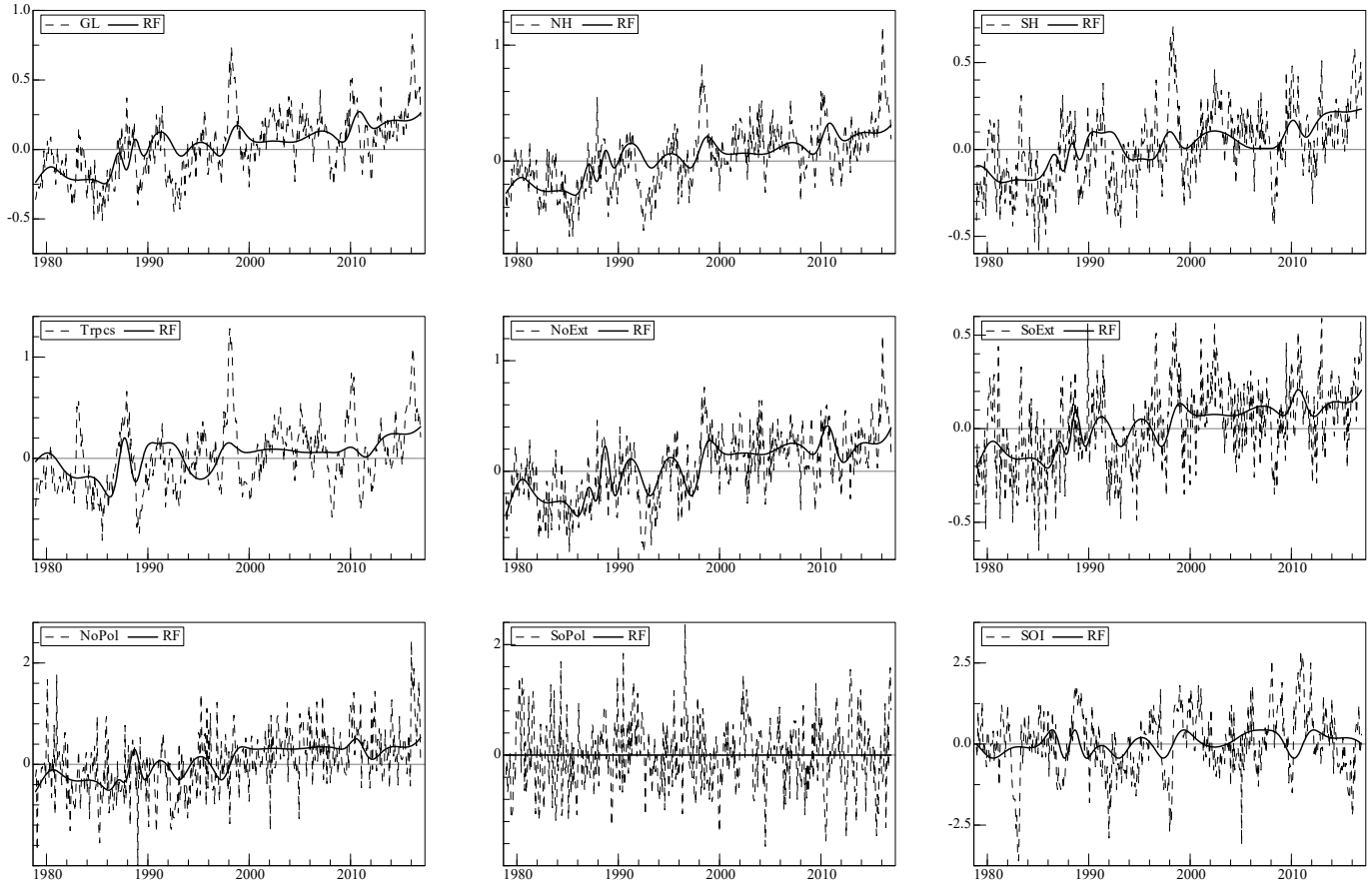

Figure 2: Temperature anomalies for the entire globe (GL; 90S-90N) and seven zones, namely the Northern Hemisphere (NH; 0-90N), the Southern Hemisphere (SH; 90S-0), the Tropics (Trpcs; 20S-20N), the Northern Extratropic (NoExt; 20N-90N), the Southern Extratropic (SoExt; 90S-20S), the Northern Polar (NoPol; 60N-90N), the Southern Polar (SoPol; 90S-60S). The Southern Oscillation Index is also plotted (SOI). For all series RF denotes the nonlinear trend associated with radiative forcing.

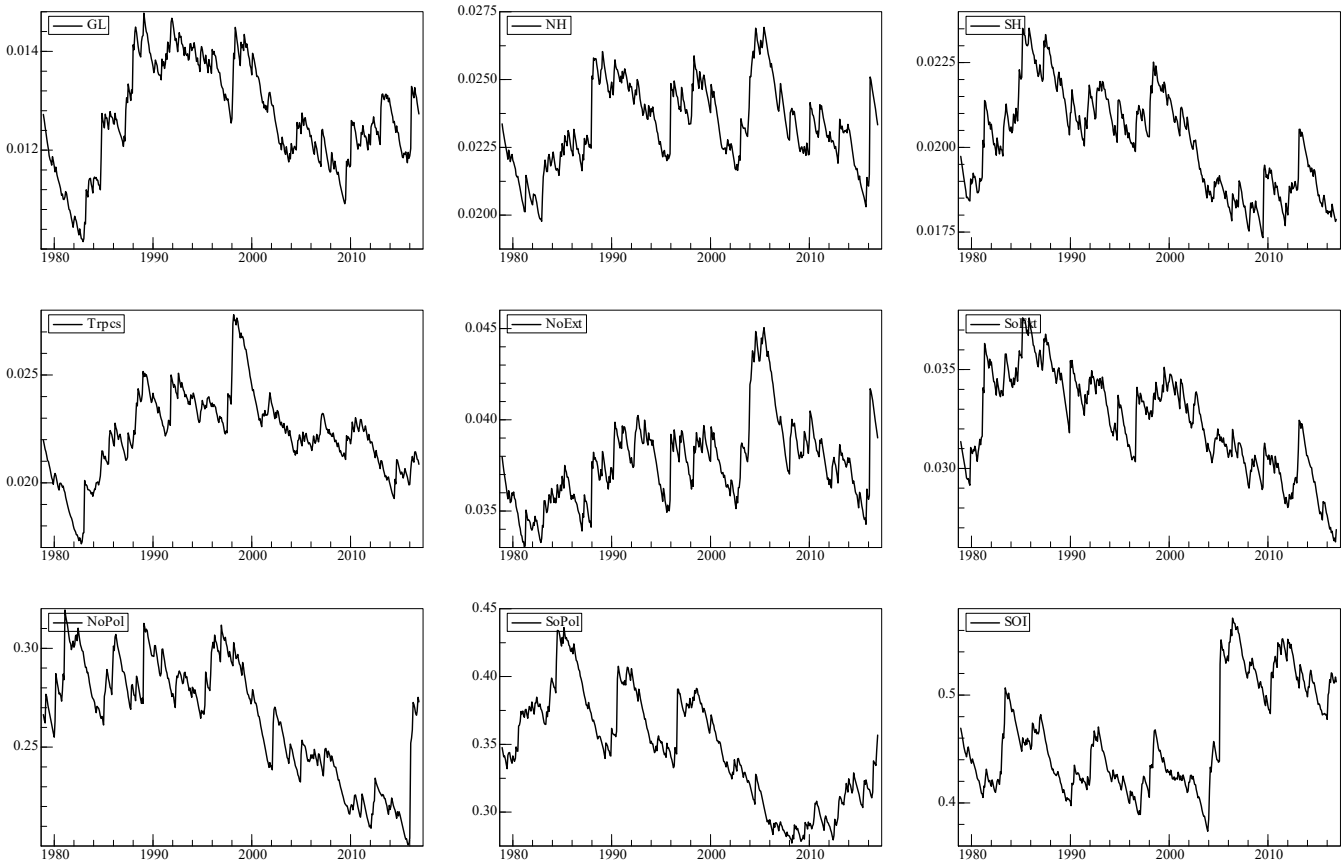

Figure 3: Estimated conditional variances of temperature anomalies for the entire globe (GL; 90S-90N) and seven zones, namely the Northern Hemisphere (NH; 0-90N), the Southern Hemisphere (SH; 90S-0), the Tropics (Trpcs; 20S-20N), the Northern Extratropic (NoExt; 20N-90N), the Southern Extratropic (SoExt; 90S-20S), the Northern Polar (NoPol; 60N-90N), the Southern Polar (SoPol; 90S-60S), the Southern Oscillation Index (SOI).

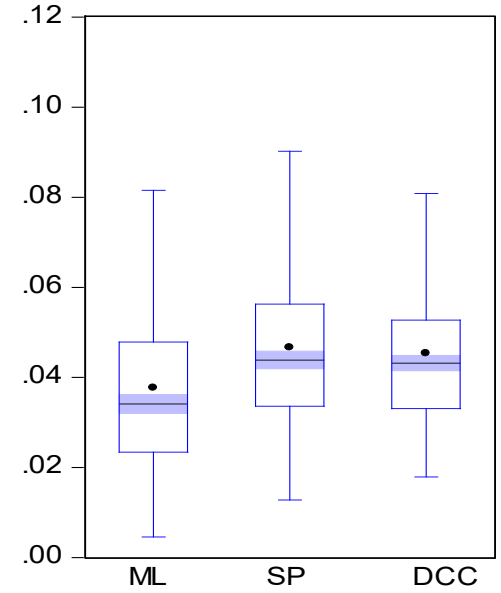

GARCH MODEL (1%)

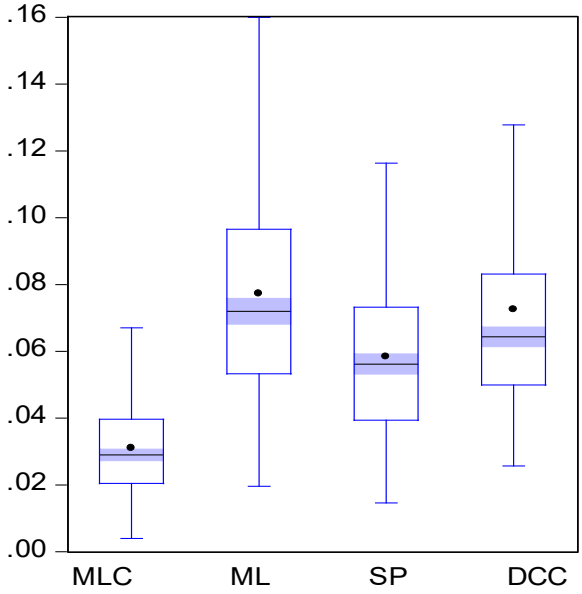

IGARCH MODEL (1%)

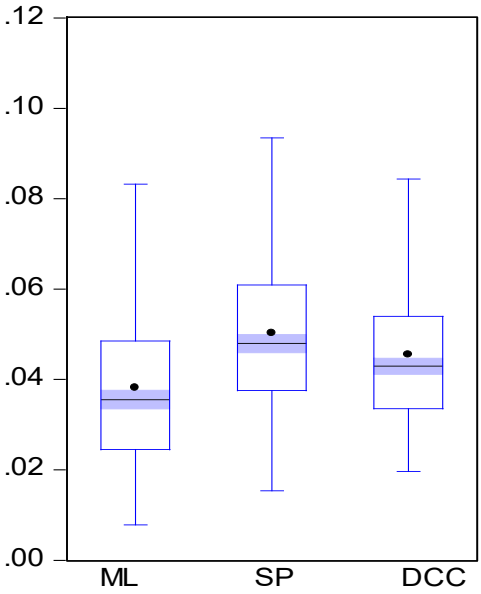

GARCH MODEL (3%)

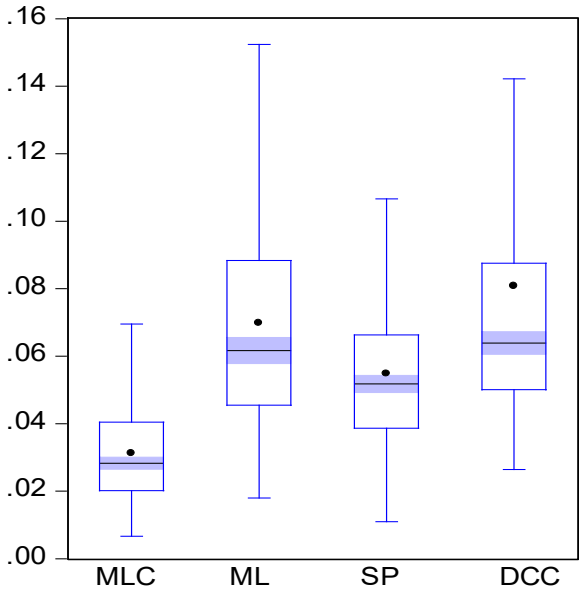

IGARCH MODEL (6%)

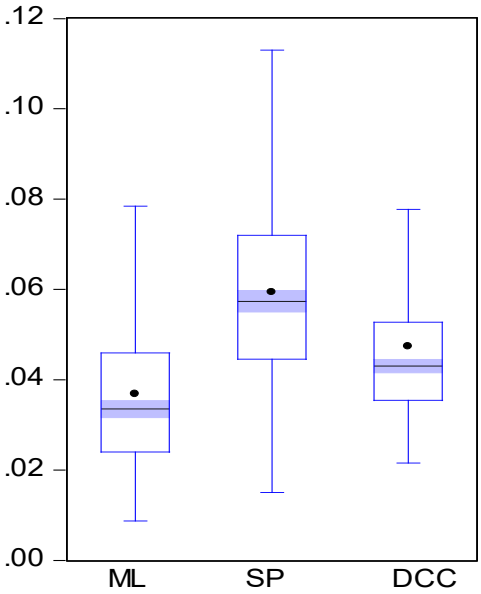

GARCH MODEL (6%)

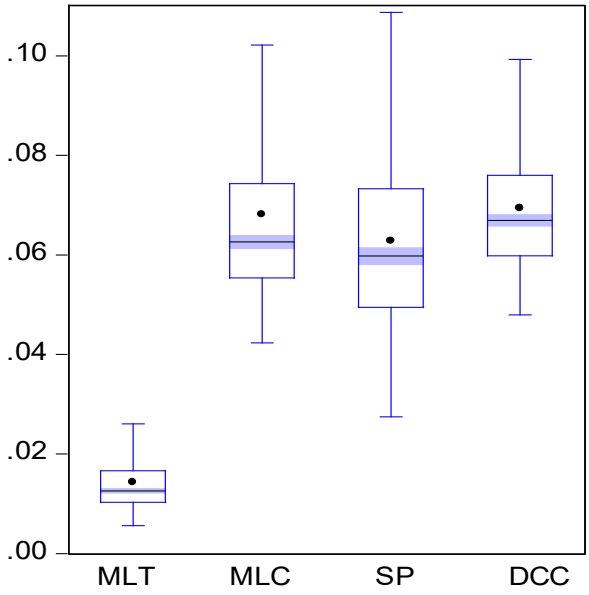

UVECH MODEL

Figure 4: Monte Carlo results. SP-DCC (SP) vs. Exact Maximum Likelihood (ML, MLT, MLC) and Engle DCC (DCC).

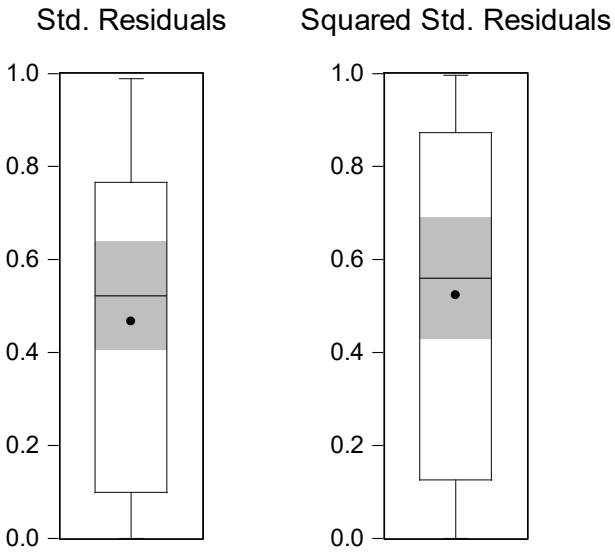

Figure 5: Boxplots for the p-values of the Box-Ljung tests carried out using standardized and squared standardized residuals.

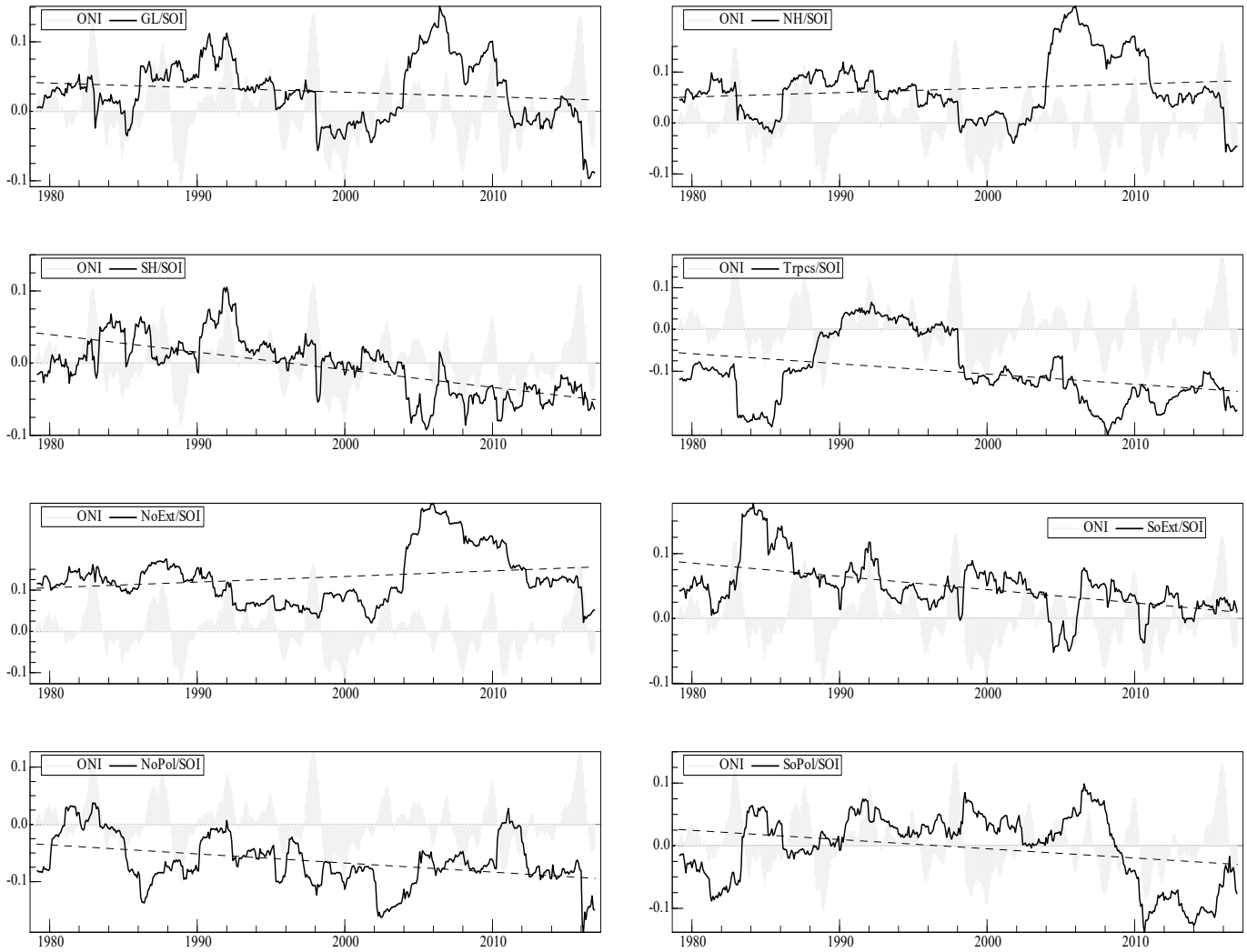

Figure 6: Estimated conditional correlations of the Southern Oscillation Index (SOI) versus various temperature anomalies: the entire globe (GL/SOI), the Northern Hemisphere (NH/SOI), the Southern Hemisphere (SH/SOI), the Tropics (Trpcs/SOI), the Northern Extratropic (NoExt/SOI), the Southern Extratropic (SoExt/SOI), the Northern Polar (NoPol/SOI), the Southern Polar (SoPol/SOI). ONI is the Oceanic Niño Index, scaled to match means and ranges of the various conditional correlations.

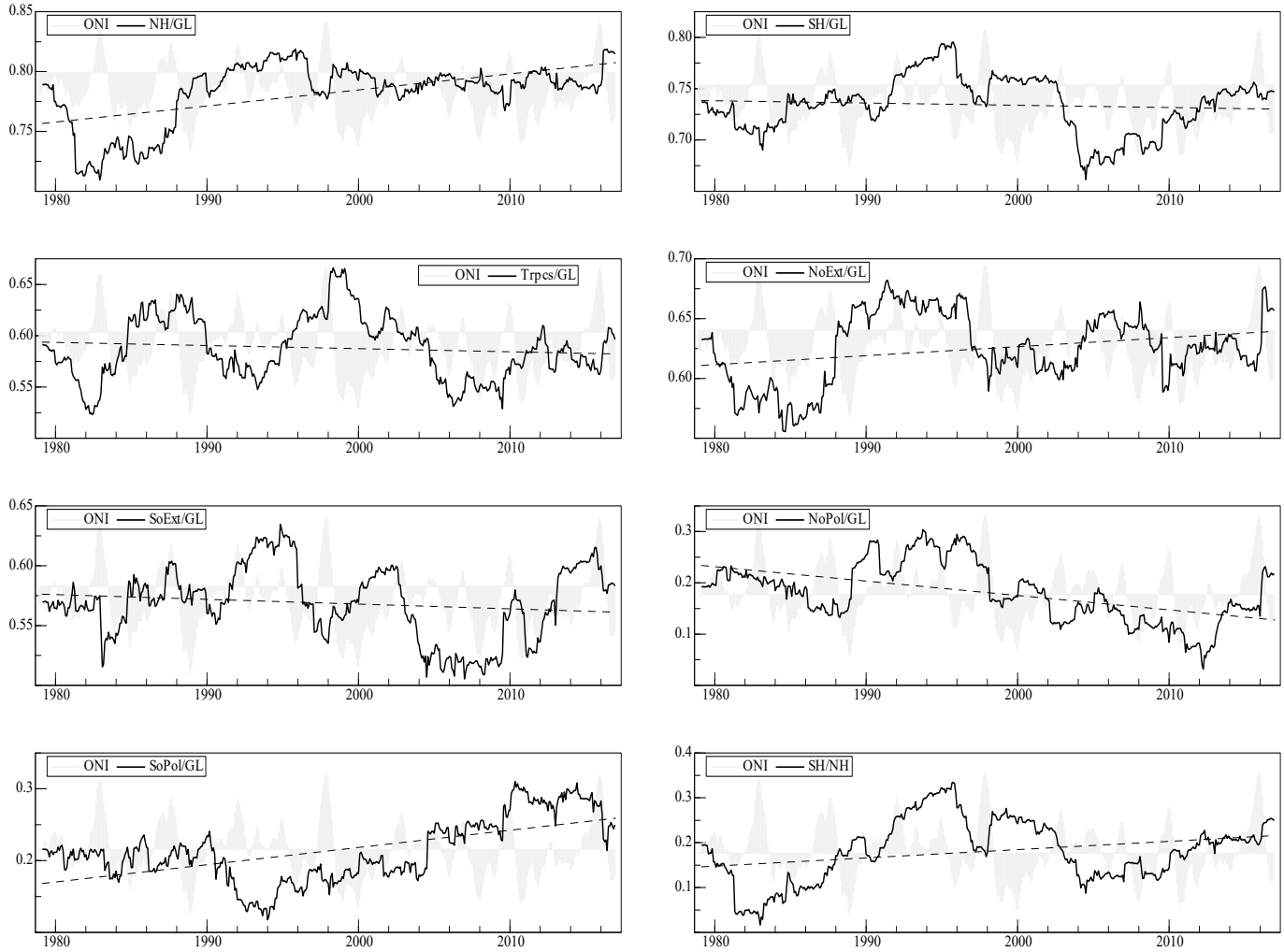

Figure 7: Estimated conditional correlations of the global temperature anomaly versus temperature anomalies of various zones: the Northern Hemisphere (NH/GL), the Southern Hemisphere (SH/GL), the Tropics (Trpcs/GL), the Northern Extratropic (NoExt/GL), the Southern Extratropic (SoExt/GL), the Northern Polar (NoPol/GL) and the Southern Polar (SoPol/GL). In the figure also the conditional correlations of the Northern Hemisphere anomaly versus the Southern Hemisphere anomaly (SH/NH) is plotted. ONI is the Oceanic Niño Index, scaled to match means and ranges of the various conditional correlations.

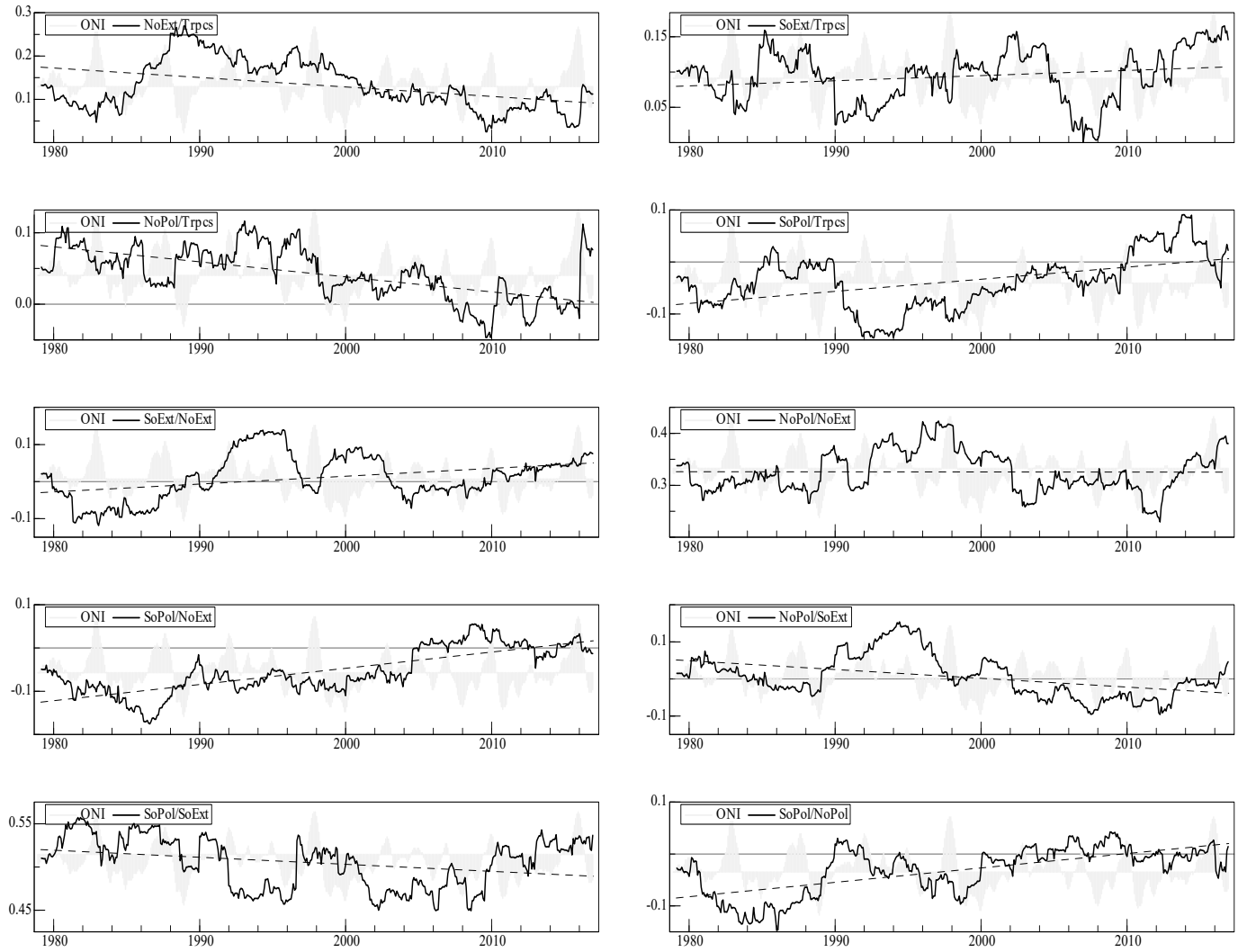

Figure 8: Conditional correlations of various temperature anomalies: Tropics versus the Northern (NoExt/Tropics) and Southern (SoExt/Trpcs) Extratropic; Tropics versus the Northern (NoPol/Trpcs) and Southern (SoPol/Trpcs) Polar. The Northern Extratropic versus the Southern Extratropic (SoExt/NoExt) and the Northern (NoPol/NoExt) and Southern (SoPol/NoExt) Polar. The Southern Extratropic versus the Northern (NoPol/SoExt) and Southern (SoPol/SoExt) Polar. The Northern Polar versus the Southern Polar (SoPol/NoPol). ONI is the Oceanic Niño Index scaled to match means and ranges of the various conditional correlations.